



# A thermodynamically consistent formulation of the pseudo-incompressible equations for atmospheric modelling with an extension to moist processes

Inauguraldissertation zur Erlangung
des Grades eines Doktors der
Naturwissenschaften am Fachbereich
Mathematik und Informatik der Freien
Universität Berlin

vorgelegt von

Warren O'Neill

Berlin, 2015

**Erstgutachter & Betreuer:**
Prof. Dr. Rupert Klein
*Institut für Mathematik,*
*Freie Universität Berlin*

**Zweitgutachter:**
Prof. Dr. Peter Spichtinger
*Institut für Physik der Atmosphäre,*
*Johannes Gutenberg Universität Mainz*

**Drittgutachterin:**
Dr. Ann Almgren
*Lawrence Berkeley National Laboratory*

**Tag der Disputation:**
8. Dezember 2014

# Contents

# Chapter 1

# Introduction

Atmospheric flows are composed of motions occurring on a large range of temporal and spatial scales. All of these motions can be captured by the compressible Navier-Stokes equations, however, as sound waves do not play an important role in these processes, it is theoretically appealing and can be numerically advantageous to remove the sound waves entirely from the governing equations.

Many "soundproof" equation sets have been developed to tackle this issue. The most well known of these are the Boussinesq equations (Boussinesq (1903)), the anelastic equations (Ogura and Phillips (1962) and Lipps and Helmer (1982)) and the pseudo-incompressible equations (Durran (1989)). These equation sets are derived by introducing different approximations into the governing equations. The Boussinesq approximation replaces the continuity equation by an incompressibility condition, the anelastic approximation disregards the time derivative of the density in the continuity equation to yield a divergence constraint and the pseudo-incompressible approximation ignores the effect of pressure perturbations on the density which also yields a divergence constraint.

In this work we will be focusing on the pseudo-incompressible approximation and we aim to extend this model in two ways. The first is to numerically implement a "thermodynamically-consistent" formulation of the pseudo-incompressible equations and the second is to extend the model to include moisture, i.e. phase changes and diabatic terms. These two aspects are outlined in more detail in the following paragraphs.

Typically, the pseudo-incompressible equations are written in "$\pi - \theta$" form i.e., with the Exner pressure $\pi$ and the potential temperature $\theta$ utilised in the momentum equation's pressure and gravity terms and not thermodynamic pressure $p$ and the density $\rho$. An outline for the latter formulation is given in Klein and Pauluis (2011) and it requires that all terms up to first order in the pressure perturbation are retained in the momentum equation which is a condition which is automatically fulfilled in the "$\pi - \theta$" case. This complicates the numerics in two ways: 1) it adds a pressure perturbation dependent source term to the momentum equation and 2) it alters the form of the projection step used to enforce the divergence constraint. A method to resolve these issues was outlined by the author in Benacchio et al. (2014) and will also be illustrated in the first part of the present work.

For the remainder we will examine the effect of moisture on our pseudo-incompressible model. So far only the anelastic equations have been utilised extensively as a basis for modelling moist flows (e.g. Clark (1977), Lipps and Helmer (1982), Grabowski and Smolarkiewicz (2002) and Pauluis (2008)). The Boussinesq equations are unsuitable for moist atmospheric applications due to the assumption of constant density and the pseudo-incompressible equations are rarely used in moist form due to the complications that latent heat causes in the divergence constraint.

In Almgren et al. (2008), a pseudo-incompressible model with source terms and compositional changes for supernovae is developed which overcomes these complications. Motivated by this work we have created a non-thermodynamically consistent pseudo-incompressible model for moist atmospheric flows which is outlined in O'Neill and Klein (2013). This entailed the derivation of a background state which varies in time as a result of the release of latent heat. The creation of such a background state solves the problems created by the heat

source in the divergence constraint and allows the pseudo-incompressible model to incorporate diabatic terms.

This model is valid for flows with large density and potential temperature variations and is therefore more generally applicable than the anelastic approximation which is only valid for small variations (as shown in Klein (2009)). In the analysis presented in Lipps and Helmer (1982), for example, they require the potential temperature to be a slowly varying function of the vertical coordinate for their moist anelastic model. If we focus on atmospheric motions then this restricts the validity of their model to motions in the troposphere and in this paper they state that "for severe mid-latitude convection...the present analysis is expected to have limited validity". However, the assumption of small density and potential temperature variations is valid for most atmospheric processes of interest and our model is advantageous only in specific cases.

Continuing the work of O'Neill and Klein (2013) further we will develop the moist model to be thermodynamically consistent. This is carried out in much the same fashion as in the dry case except the background variables in the gravity term will now be functions of time as well as height. Moreover, inspired by the work presented in Kurowski et al. (2013) we will examine the effect of the pressure choice used, full value or hydrostatic, for the condensation rate calculation.

To implement our models numerically we have incorporated it into an in-house finite volume code for low Mach number flow based on the numerics found in Klein (2009). The models are then verified against a number of testcases which are used to examine various aspects of the interest, e.g. how the model performs under buoyancy driven flow.

In summary, the thesis will have the following outline: we begin with a derivation, starting from the compressible equations, of the dry thermodynamically consistent set. This is followed by a derivation of the moist form of the thermodynamically consistent set. The numerics used for modelling each set of equations is then outlined and finally each model is tested and compared using several standard dry and moist testcases.

Chapter 2

# Thermodynamically consistent pseudo-incompressible equations

## 2.1 Background to the pseudo-incompressible equations

Sound waves occur in a medium due to the influence of pressure fluctuations on the density. The family of soundproof models make various approximations to the density equation in order to remove this influence and, thus, to filter soundwaves. In the case of the pseudo-incompressible approximation the density is assumed to be independent from perturbations in pressure but remain dependent on temperature perturbations.

Traditionally, the pseudo-incompressible model is derived from a compressible model formulated using the Exner pressure in the momentum equation. For a dry atmosphere the Exner pressure $\pi$ is defined as

$$\pi = \left(\frac{p}{p_{ref}}\right)^{R/c_p} \tag{2.1}$$

where $p$ is the thermodynamic pressure, $p_{ref}$ is the reference pressure, $R$ is the dry gas constant and $c_p$ is the dry specific heat capacity at a constant pressure. When the Exner pressure is utilised, as in the original pseudo-incompressible derivation presented in Durran (1989), the momentum equation has the advantage that it is independent of density when written in conservative form. This means that any approximation made to the density will not have an effect on the momentum equation.

In this work, however, we will build a pseudo-incompressible model whose momentum equation is composed using the standard thermodynamic pressure $p$ rather than $\pi$. In this case the momentum equation is not independent of density even when written in non-conservative form. As a result, great care must be taken to ensure that the pseudo-incompressible approximation retains the original form of the momentum equation to, at least, first order in pressure. The correct way to do this for general equations of state was outlined in Klein and Pauluis (2011) and requires the retention of the effect of pressure perturbations in the buoyancy term. In the current chapter we will show how the aforementioned general method can be applied to a specific regime.

Deriving the pseudo-incompressible equations in this way is thought to have several advantages. For example, it is potentially easier to extend the model to incorporate more general equations of state since the Exner formulation would require extra terms in the momentum equation which, e.g., depend on the derivatives of the species. Even for non-complex equations of state $p - \rho$ formulation has the advantage that the pressure term in the momentum equation is written in conservative form. This has the numerical advantage that the pressure in the momentum equation can be written as an exact flux and will thus improve the conservation properties of the momentum.

## 2.2 Derivation of the thermodynamically consistent pseudo-incompressible equations

### 2.2.1 The compressible equations

We will use the two dimensional non-rotational compressible Euler equations for a single fluid given in Klein and Pauluis (2011) as the starting point for our derivation. For this equation set the density and momentum equation are given as

$$\rho_t + \nabla \cdot (\rho \mathbf{u}) = 0 \tag{2.2}$$

$$\mathbf{u}_t + \cdot \nabla \mathbf{u} + \frac{1}{\rho} \nabla p = -g\mathbf{k} \tag{2.3}$$

where the $t$ subscript signifies the partial derivative with respect to time $t$, $\rho$ is the fluid density, $\mathbf{u}$ is the two dimensional velocity vector, $g$ is the gravitational acceleration, $\mathbf{k}$ is the unit vertical vector and the equations operate on the domain $\Omega = [x_{min}, x_{max}] \times [0, z_{max}]$.

We have yet to define an "energy" equation for the system and we will do this by using the potential temperature variable. We define the potential temperature and ideal gas equations as

$$\theta = T(p_{ref}/p)^{(R/c_p)} \tag{2.4}$$

$$p = \rho R T \tag{2.5}$$

where $T$ is the temperature. The prognostic equation for potential temperature will be given as

$$\theta_t + \mathbf{u} \cdot \nabla \theta = 0. \tag{2.6}$$

Using (2.4) and (2.5) we can write a new equation of state for our system in terms of $\rho$, $p$ and $\theta$ as

$$\rho = \frac{1}{\theta} \frac{p_{ref}}{R} \left( \frac{p}{p_{ref}} \right)^{1/\gamma} \tag{2.7}$$

where $\gamma = c_p/c_v$. Equations (2.6)-(2.7) taken with equations (2.2)-(2.3) are the governing equations for the compressible system.

### 2.2.2 The pseudo-incompressible approximation

As in the pseudo-incompressible derivation presented in Durran (1989) we will start by assuming that the pressure does not vary much from its hydrostatic background value and can be written as

$$p = p_0(z) + p'(\mathbf{x}, t) \tag{2.8}$$

where $p'/p_0 << 1$ and

$$\frac{\partial p_0}{\partial z} = -\rho_0 g \tag{2.9}$$

for a hydrostatically balanced density $\rho_0$. The assumption of small variations in the pressure perturbation limits of the range of validity of the pseudo-incompressible but the applicability is retained for most meteorological cases of interest. For example, in Kurowski et al. (2013) they state that for their test-cases with typical atmospheric conditions they get a variation of $p'/p_0 \approx 0.0001$ but in extreme cases such as a tornado the variation can reach $p'/p_0 \approx 0.1$.

Using (2.8) and the equation of state (2.7) we can expand the density in terms of pressure perturbations and drop the higher order terms

$$\begin{aligned}\rho &= \frac{1}{\theta}\frac{p_{ref}}{R}\left(\frac{p_0+p'}{p_{ref}}\right)^{1/\gamma} \approx \frac{1}{\theta}\frac{p_{ref}}{R}\left(\frac{p_0}{p_{ref}}\right)^{1/\gamma}\left(1+\frac{p'}{\gamma p_0}\right)\\ &= \rho^*\left(1+\frac{p'}{\gamma p_0}\right)\end{aligned} \tag{2.10}$$

where $\rho^*$ is called the "pseudo-density" and is defined as the density calculated at the background pressure but using the full potential temperature, i.e.

$$\rho^* = \frac{1}{\theta}\frac{p_{ref}}{R}\left(\frac{p_0}{p_{ref}}\right)^{1/\gamma} = \rho(p_0,\theta). \tag{2.11}$$

Now, in order to filter sound waves we must suppress the effect of pressure perturbations in the conservation of mass (2.2). Inserting (2.10) into (2.2) results in the following equation for the pseudo-density

$$(\rho^*)_t + \nabla\cdot(\rho^*\mathbf{u}) = 0. \tag{2.12}$$

However, in the momentum equation we want to keep the effects of the pressure perturbations up to first order since we want to remove the effect of pressure perturbations on the density only. Using a similar expansion as in (2.10) we can re-write (2.3) as

$$\mathbf{u}_t + \mathbf{u}\cdot\nabla\mathbf{u} + \frac{1}{\rho^*}\left(1-\frac{p'}{\gamma p_0}\right)\nabla(p_0+p') = -g\mathbf{k} \tag{2.13}$$

Keeping all terms in (2.13) up to first order in the pressure perturbation, using the hydrostatic balance (2.9) and re-arranging we get

$$\mathbf{u}_t + \mathbf{u}\cdot\nabla\mathbf{u} + \frac{1}{\rho^*}\nabla(p_0+p') = -\left(1+\frac{1}{\rho^*}\frac{\rho_0}{\gamma p_0}p'\right)g\mathbf{k}. \tag{2.14}$$

Lastly, the potential potential temperature equation remains unchanged as it does not contain the density.

We will now re-write our governing equations in conservative form by multiplying the momentum and potential temperature equations by $\rho^*$ to get

$$(\rho^*\mathbf{u})_t + \nabla(\rho^*\mathbf{u}\circ\mathbf{u}) + \nabla p = -\left(\rho^* + \frac{\rho_0}{\gamma p_0}p'\right)g\mathbf{k} \tag{2.15}$$

$$(\rho^*\theta)_t + \nabla\cdot(\rho^*\theta\mathbf{u}) = 0 \tag{2.16}$$

Since $\rho^*\theta$ is a function of $p_0$ only and $p_0$ does not depend on $t$ we can drop the time derivative term from (2.16) and we can re-write the evolution equation for $\theta$ as the following divergence constraint

$$\nabla\cdot(\rho^*\theta\mathbf{u}) = 0. \tag{2.17}$$

This constraint imposes the pseudo-incompressible form of the density equation given by (2.12) thereby filtering the effect of pressure perturbations on the density and, as a result, filtering the propagation of soundwaves.

Finally, the complete pseudo-incompressible governing equations are given by

$$(\rho^*)_t + \nabla \cdot (\rho^* \mathbf{u}) = 0 \tag{2.18}$$

$$(\rho^* \mathbf{u})_t + \nabla \cdot (\rho^* \mathbf{u} \circ \mathbf{u}) + \nabla p = -\left(\rho^* + \frac{\rho_0}{\gamma p_0} p'\right) g\mathbf{k} \tag{2.19}$$

$$\nabla \cdot (P\mathbf{u}) = 0 \tag{2.20}$$

where

$$P = \rho^* \theta = \frac{p_{ref}}{R} \left(\frac{p}{p_{ref}}\right)^{1/\gamma}. \tag{2.21}$$

Comparing (2.18)-(2.20) to an anelastic equation set, e.g. Lipps and Helmer (1982), we see that the differences are seen in the density. In the anelastic equations the density is set to the initial hydrostatic values whereas here the less restrictive "pseudo-density" is used.

### 2.2.3 Comparing $\pi - \theta$ and $p - \rho$ formulations

In this section we will show the equivalence of the traditional $\pi - \theta$ formulation of the pseudo-incompressible equations presented in Durran (1989) and the thermodynamic consistent $p - \rho$ formulation. A similar derivation to the one presented here is given in Klein et al. (2013).

To start, we will write $P$ and $\pi$ as expansions in pressure

$$\begin{aligned} P =& \frac{p_{ref}}{R} \left(\frac{p}{p_{ref}}\right)^{\frac{1}{\gamma}} = \frac{p_{ref}}{R} \left(\frac{p_0 + p'}{p_{ref}}\right)^{\frac{1}{\gamma}} = \frac{p_{ref}}{R} \left(\frac{p_0}{p_{ref}}\right)^{\frac{1}{\gamma}} \left(1 + \frac{p'}{p_0}\right)^{\frac{1}{\gamma}} \\ \approx& \frac{p_{ref}}{R} \left(\frac{p_0}{p_{ref}}\right)^{\frac{1}{\gamma}} \left(1 + \frac{p'}{\gamma p_0}\right) + \mathrm{O}\big(p'^2\big) = P_0 \left(1 + \frac{p'}{\gamma p_0}\right) + \mathrm{O}\big(p'^2\big) \end{aligned} \tag{2.22}$$

and

$$\begin{aligned} \pi =& \left(\frac{p}{p_{ref}}\right)^{\frac{\gamma-1}{\gamma}} = \left(\frac{p_0 + p'}{p_{ref}}\right)^{\frac{\gamma-1}{\gamma}} = \left(\frac{p_0}{p_{ref}}\right)^{\frac{\gamma-1}{\gamma}} \left(1 + \frac{p'}{p_0}\right)^{\frac{\gamma-1}{\gamma}} \\ \approx& \frac{p_0}{p_{ref}} \left(\frac{p_0}{p_{ref}}\right)^{-\frac{1}{\gamma}} \left(1 + \frac{\gamma - 1}{\gamma} \frac{p'}{p_0}\right) + \mathrm{O}\big(p'^2\big) \\ =& \frac{p_0}{p_{ref}} \frac{p_{ref}}{P_0 R} \left(1 + \frac{R}{c_p} \frac{p'}{p_0}\right) + \mathrm{O}\big(p'^2\big) = \frac{p_0}{R P_0} + \frac{p'}{c_p P_0} + \mathrm{O}\big(p'^2\big) \\ =& \pi_0 + \pi' + \mathrm{O}\big(p'^2\big) \end{aligned} \tag{2.23}$$

where

$$\pi_0 = \frac{p_0}{R P_0} \tag{2.24}$$

and

$$\pi' = \frac{p'}{c_p P_0}. \tag{2.25}$$

The standard pseudo-incompressible momentum equation in $\pi - \theta$ form taken from Durran (1989) is written in conservation form as

$$(\rho^* \mathbf{u})_t + \nabla \cdot (\rho^* \mathbf{u} \circ \mathbf{u}) + c_p P_0 \nabla \pi = -\rho^* g \mathbf{k} \tag{2.26}$$

Using the expansion of $\pi$ in (2.23) we can re-write (2.26) as

$$\begin{aligned}
(\rho^* \mathbf{u})_t + \nabla \cdot (\rho^* \mathbf{u} \circ \mathbf{u}) &= - c_p P_0 \nabla \pi - \rho^* g \mathbf{k} \\
&= - c_p \nabla \left( P_0 \pi \right) + c_p \pi \nabla P_0 - \rho^* g \mathbf{k} \\
&= - c_p \nabla \left( \frac{p_0}{R} - \frac{p'}{c_p} \right) + c_p \pi \frac{P_0}{\gamma p_0} \nabla p_0 - \rho^* g \mathbf{k} \\
&= - \frac{c_p}{R} \nabla p_0 - \nabla p' - \left( \frac{c_p p_0}{R P_0} + \frac{p'}{P_0} \right) \frac{P_0}{\gamma p_0} \nabla p_0 - \rho^* g \mathbf{k} \\
&= - \frac{c_p}{R} \nabla p_0 + \nabla p' + \left( \frac{c_p}{\gamma R} + \frac{p'}{\gamma p_0} \right) \nabla p_0 - \rho^* g \mathbf{k} \\
&= - \nabla (p_0 + p') - \frac{\rho_0 g}{\gamma p_0} p' \mathbf{k} - \rho^* g \mathbf{k}
\end{aligned} \tag{2.27}$$

where in the last inequality we have used the hydrostatic balance and the fact that $\frac{c_p}{R}\left(1 - 1/\gamma\right) = 1$. We can re-arrange (2.27) to give us the equation utilised for our pseudo-incompressible model in $p - \rho$ form

$$(\rho^* \mathbf{u})_t + \nabla \cdot (\rho^* \mathbf{u} \circ \mathbf{u}) + \nabla p = - \left( \rho^* + \frac{\rho_0}{\gamma p_0} p' \right) g \mathbf{k} \tag{2.28}$$

where $p = p_0 + p'$.

Chapter 3

# A moist pseudo-incompressible model

## 3.1 Background to the moist pseudo-incompressible equations

The use of moist soundproof models is sparse when compared with their dry counterparts. Although EULAG users (see Smolarkiewicz and Charbonneau (2013)) have been documenting the use of their soundproof anelastic model in a moist setting the usage of moist pseudo-incompressible models is relatively unheard of. The reasons for this are, perhaps, the extra difficulties that such a formulation encounters. These difficulties stem from the fact that the divergence constraint is derived from the energy equation and is thus affected greatly by the heating sinks and sources encountered in moist physics. This issue is not present in the anelastic model, however, due to the fact that the divergence constraint is derived from the density equation which is free of source terms.

To tackle these unique obstacles we proposed a method outlined in O'Neill and Klein (2013) which was motivated by the work on low Mach number modelling of supernovae presented in Almgren et al. (2008). Unlike the dry case in the previous chapter, the method requires the definition of a background state which varies in both time and height and a derivation of a governing set of equations for such a state.

The model presented in O'Neill and Klein (2013) is not thermodynamically consistent, however, and in this section we would like to incorporate the methods of Klein and Pauluis (2011) to create a pseudo-incompressible model which captures moist processes and is thermodynamically consistent. Extending the model to be thermodynamically consistent is carried out in much the same fashion as illustrated in Chapter 2 except in the moist case the extra buoyancy term which necessitates thermodynamic consistency will have hydrostatic terms that are now functions of time. This extra buoyancy term is the difference between the model presented in this chapter and the model present in O'Neill and Klein (2013).

## 3.2 Derivation of the moist pseudo-incompressible equations

### 3.2.1 Model assumptions

We will be making several assumptions in our model, namely, the model contains only three phases (dry air, water vapour, cloud water), each phase will have the same temperature and velocity field, we will be ignoring hydrometeor fallout, ice-phase micro-physics, the Coriolis force, sub-grid-scale turbulence and we will assume solid-wall (or periodic) horizontal boundary conditions and solid-wall vertical boundary conditions.

### 3.2.2 The moist compressible equations

Making the above mentioned assumptions we arrive at the following two dimensional compressible equations with bulk microphysics as presented in Bryan and

Fritsch (2002)

$$\rho_t + \nabla \cdot (\rho \mathbf{u}) = 0 \tag{3.1}$$

$$\mathbf{u}_t + \mathbf{u} \cdot \nabla \mathbf{u} + \frac{1}{\rho} \nabla p = -g\mathbf{k} \tag{3.2}$$

$$(q_v)_t + \mathbf{u} \cdot \nabla q_v = -C \tag{3.3}$$

$$(q_c)_t + \mathbf{u} \cdot \nabla q_c = C \tag{3.4}$$

where the $\rho$ is the total density, $q_v$ is the vapour mixing ratio, $q_c$ is the cloud water mixing ratio, $C$ is condensation rate and the equations operate on the domain $\Omega = [x_{min}, x_{max}] \times [0, z_{max}]$. Note, the total density is written as

$$\rho = \rho_a (1 + q_v + q_c) \tag{3.5}$$

where $\rho_a$ is the dry air density.

As in the dry model we will use the potential temperature to define our "energy" equation. The potential temperature and ideal gas equations of state are given as

$$\theta = T(p_{ref}/p)^{(R/c_p)} \tag{3.6}$$

$$p = \rho_a RT + \rho_v R_v T = \left( \frac{1 + q_v/\epsilon}{1 + q} \right) \rho RT \tag{3.7}$$

where $R$ and $c_p$ are equal to the dry values, $R_v$ is the vapour gas constant, $\epsilon = R/R_v$ and $q = q_v + q_c$ is the total mixing ration. Note, the only difference compared to the dry equations of state is the term in brackets on the right hand side of (3.7).

The prognostic equation for potential temperature is given as

$$\theta_t + \mathbf{u} \cdot \nabla \theta = \frac{\theta L_v}{c_p T} C \tag{3.8}$$

where $L_v$ is the latent heat of vaporization and is defined differently for each testcase (see Appendix B). To simplify the derivation we will rewrite (3.8) using a new variable $\theta_q$ defined as $\theta_q = \left( \frac{1+q_v/\epsilon}{1+q} \right) \theta$. Combining (3.3), (3.4) and (3.8) we get the following equation for $\theta_q$

$$(\theta_q)_t + \mathbf{u} \cdot \nabla \theta_q = \left[ L_v/c_p T - 1/(\epsilon + q_v) \right] \theta_q C. \tag{3.9}$$

Using (3.6) and (3.7) we can write $\rho$ in terms of $p$ as $\theta_q$ as

$$\rho = \frac{1}{\theta_q} \frac{p_{ref}}{R} \left( \frac{p}{p_{ref}} \right)^{1/\gamma} \tag{3.10}$$

Equation (3.9) taken with equations (3.1)-(3.4) are the governing equations for the moist compressible system and are our starting point for the derivation of the moist pseudo-incompressible equations.

### 3.2.3 The moist pseudo-incompressible approximation

As in the dry pseudo-incompressible derivation presented in Chapter 2 we will start by assuming that the pressure does not vary much from its hydrostatic background value and can be written as

$$p = p_0(z,t) + p'(\mathbf{x},t) \tag{3.11}$$

where $p'/p_0 << 1$ and

$$\frac{\partial p_0}{\partial z} = -\rho_0 g. \tag{3.12}$$

Note, that unlike in the dry case we have allowed the hydrostatic values to vary in time as in Almgren et al. (2008). This will solve the problem presented by the latent heat term in the divergence constraint by allowing the changing background state to compensate for the heating effect. In the idealised dry testcase presented in Almgren (2000) the changing background state was shown to play a vital role in ensuring that the solution converges to the compressible solution in the limit of a small heating rate.

If we expand the pressure in equation (3.10) we get

$$\begin{aligned}\rho =& \frac{1}{\theta_q}\frac{p_{ref}}{R}\left(\frac{p_0+p'}{p_{ref}}\right)^{1/\gamma} = \frac{1}{\theta_q}\frac{p_{ref}}{R}\left(\frac{p_0}{p_{ref}}\right)^{1/\gamma}\left(1+\frac{p'}{p_0}\right)^{1/\gamma} \\ \approx& \frac{1}{\theta_q}\frac{p_{ref}}{R}\left(\frac{p_0}{p_{ref}}\right)^{1/\gamma}\left(1+\frac{p'}{\gamma p_0}\right) = \rho^*\left(1+\frac{p'}{\gamma p_0}\right)\end{aligned} \tag{3.13}$$

where

$$\rho^* = \frac{1}{\theta_q}\frac{p_{ref}}{R}\left(\frac{p_0}{p_{ref}}\right)^{1/\gamma} = \rho(p_0,\theta_q). \tag{3.14}$$

Now, in order to filter sound waves we drop the terms in the conservation of mass which depend on the pressure perturbation and we get the following equation for the pseudo-density

$$(\rho^*)_t + \nabla\cdot(\rho^*\mathbf{u}) = 0. \tag{3.15}$$

In the momentum equation we want to keep the effect of the pressure perturbation and using a similar method to the expansion in (3.13) we can re-write (3.2) as

$$\mathbf{u}_t + \mathbf{u}\cdot\nabla\mathbf{u} + \frac{1}{\rho^*}\left(1-\frac{p'}{\gamma p_0}\right)\nabla(p_0+p') = -g\mathbf{k}. \tag{3.16}$$

Keeping all terms in (3.16) up to first order in the pressure perturbation and re-arranging we get

$$\mathbf{u}_t + \mathbf{u}\cdot\nabla\mathbf{u} + \frac{1}{\rho^*}\nabla(p_0+p') = -\left(1+\frac{1}{\rho^*}\frac{\rho_0}{\gamma p_0}p'\right)g\mathbf{k}. \tag{3.17}$$

Lastly, $\theta_q$ remains unchanged as it does not contain the density.

We will now re-write our governing equations in conservative form by multiplying the momentum (3.17), species (3.3)-(3.4) and potential temperature (3.9) equations by $\rho^*$ to get

$$(\rho^*\mathbf{u})_t + \nabla(\rho^*\mathbf{u}\circ\mathbf{u}) + \nabla p = -\left(\rho^* + \frac{\rho_0}{\gamma p_0}p'\right)g\mathbf{k} \tag{3.18}$$

$$(\rho^* q_v)_t + \nabla\cdot(\rho^* q_v\mathbf{u}) = -\rho^* C \tag{3.19}$$

$$(\rho^* q_c)_t + \nabla\cdot(\rho^* q_c\mathbf{u}) = \rho^* C \tag{3.20}$$

$$(\rho^*\theta_q)_t + \nabla(\rho^*\theta_q\mathbf{u}) = S \tag{3.21}$$

where $S = \left[L_v/c_pT - 1/(\epsilon+q_v)\right]\rho^*\theta_q C$.

Now, since $\rho^*\theta_q$ is a function of $p_0$ only we can re-write the evolution equation (3.21) as the following divergence constraint

$$\nabla\cdot(P_0\mathbf{u}) = S - (P_0)_t \tag{3.22}$$

where

$$P_0(z,t) = \rho^*\theta_q = \frac{p_{ref}}{R}\left(\frac{p_0}{p_{ref}}\right)^{1/\gamma}. \tag{3.23}$$

As in the dry case, the constraint in (3.22) imposes the pseudo-incompressible form of the density equation given by (3.15) thereby filtering the effect of pressure perturbations on the density and, as a result, filtering the propagation of soundwaves. However, we still must derive an evolution equation for $P_0$ to evaluate the time derivative on the right hand side of (3.22).

### 3.2.4 Evolution of the background state

Following the methods of Almgren et al. (2008) we let $\mathbf{u} = \tilde{\mathbf{u}} + w_0\mathbf{k}$, where $w_0$ is the base-state velocity and $\tilde{\mathbf{u}}$ governs the remaining local dynamics such that

$$\int_{x_{min}}^{x_{max}} \tilde{\mathbf{u}}.\mathbf{k}\,\mathrm{d}x = 0. \tag{3.24}$$

This means that the domain-wide changes in the vertical flux due to heating are entirely incorporated into $w_0$. We will also assume the hydrostatic density satisfies the continuity equation, i.e.

$$(\rho_0)_t + \frac{\partial\rho_0 w_0}{\partial z} = 0. \tag{3.25}$$

The implications of this assumption are discussed in Appendix A.

Using equation (3.22) and assuming solid-wall (or periodic) horizontal boundary conditions we can derive the following equation for the background state by integrating across the horizontal domain to get

$$(P_0)_t + \frac{\partial P_0 w_0}{\partial z} = \overline{S} \tag{3.26}$$

where $\bar{\cdot} = \frac{1}{L}\int_{x_{min}}^{x_{max}} \cdot \, \mathrm{d}x$. Using (3.23) we rewrite equation (3.26) as

$$(P_0)_t + \frac{\partial P_0 w_0}{\partial z} = \frac{\partial P_0}{\partial p_0}\frac{\overline{D}p_0}{\overline{D}t} + P_0\frac{\partial w_0}{\partial z} = P_0\left(\frac{1}{\gamma p_0}\frac{\overline{D}p_0}{\overline{D}t} + \frac{\partial w_0}{\partial z}\right) = \overline{S} \tag{3.27}$$

where the background material derivative $\frac{\overline{D}}{\overline{D}t}$ is defined as $\frac{\overline{D}}{\overline{D}t} = \frac{\partial}{\partial t} + w_0\frac{\partial}{\partial z}$.

Now, in order to calculate $w_0$ we need to obtain a value for the material derivative of the background pressure. To do this we first integrate the hydrostatic balance (3.12) from any height $z \in [0, z_{max}]$ to the top of the domain $z = z_{top}$ to get

$$p_0^{top}(t) - p_0(z,t) = -\int_z^{z_{top}} \rho_0(z',t) g \, \mathrm{d}z' \tag{3.28}$$

where $p_0^{top}(t) = p_0(z_{top}, t)$. We now take the background material derivative of (3.28) to get

$$\begin{aligned}\frac{\overline{D}p_0}{\overline{D}t} =& \frac{\partial p_0^{top}}{\partial t} + \frac{\overline{D}}{\overline{D}t}\int_z^{z_{top}} \rho_0(z',t) g \, \mathrm{d}z' \\ =& \frac{\partial p_0^{top}}{\partial t}\end{aligned} \tag{3.29}$$

where $\frac{\overline{D}}{\overline{D}t}\int_z^{z_{top}} \rho_0(z',t) g \, \mathrm{d}z' = 0$ due to the fact that the weight of the columns in the background state do not change according to (3.25) and due to the fact that we are using solid-wall vertical boundary conditions.

It also possible to derive a model which utilises an open-top boundary condition which would be more common for meteorological applications. This can be achieved following the method presented in Almgren et al. (2008) more closely by assuming the pressure of a parcel does not change, i.e. $\frac{\overline{D}p_0}{\overline{D}t} = 0$, rather than assuming that the weight of the columns do not change as done above. This assumption is then used in (3.27) to derive an equation for $w_0$. Also, a suitable buffer layer would have to be implemented to damp spurious motions approaching the upper boundary.

Inserting (3.29) into (3.27) and integrating from the bottom to the top of the domain in the $z$ direction and re-arranging we get

$$\frac{\partial p_0^{top}}{\partial t} = \frac{\int_{z_{min}}^{z_{max}} \overline{S}/P_0 \, \mathrm{d}z}{\int_{z_{min}}^{z_{max}} 1/\gamma p_0 \, \mathrm{d}z}. \tag{3.30}$$

Now that we have a value for $\frac{\partial p_0^{top}}{\partial t}$ we can calculate $w_0$ by integrating (3.27) from $z = z_{min}$ to $z$ to get a value for the background velocity at height $z$

$$w_0 = \int_{z_{min}}^{z} \left(\frac{\overline{S}}{P_0} - \frac{1}{\gamma p_0}\frac{\partial p_0^{top}}{\partial t}\right) \mathrm{d}z'. \tag{3.31}$$

The background velocity $w_0$ can then be used to determine $(P_0)_t$ using the evolution equation (3.26) and $(P_0)_t$ can then be used to solve the divergence constraint (3.22).

### 3.2.5 The moist pseudo-incompressible equations

Here we will present the full set of governing equations. The evolution equations for the full values are given by

$$\rho^*_t + \nabla \cdot (\rho^* \mathbf{u}) = 0 \tag{3.32}$$

$$(\rho^* \mathbf{u})_t + \nabla \cdot (\rho^* \mathbf{u} \circ \mathbf{u})) + \nabla p = -\left(\rho^* + \frac{\rho_0}{\gamma p_0} p'\right) g\mathbf{k} \tag{3.33}$$

$$(\rho^* q_v)_t + \nabla \cdot (\rho^* q_v \mathbf{u}) = -\rho^* C \tag{3.34}$$

$$(\rho^* q_c)_t + \nabla \cdot (\rho^* q_c \mathbf{u}) = \rho^* C. \tag{3.35}$$

We also have the following equations for the background state

$$\frac{\partial \rho_0}{\partial t} + \frac{\partial \rho_0 w_0}{\partial z} = 0 \tag{3.36}$$

$$\frac{\partial P_0}{\partial t} + \frac{\partial P_0 w_0}{\partial z} = \overline{S} \tag{3.37}$$

$$\frac{\partial p_0^{top}}{\partial t} = \frac{\int_{z_{min}}^{z_{max}} \overline{S}/P_0 \, \mathrm{d}z}{\int_{z_{min}}^{z_{max}} 1/\gamma p_0 \, \mathrm{d}z} \tag{3.38}$$

$$w_0(z,t) = \int_{z_{min}}^{z} \left(\frac{\overline{S}}{P_0} - \frac{1}{\gamma p_0} \frac{\partial p_0^{top}}{\partial t}\right) \mathrm{d}z' \tag{3.39}$$

and the following equation of state and divergence constraint

$$P_0 = \left(\frac{1 + q_v/\epsilon}{1+q}\right) \rho^* \theta = \frac{p_{ref}}{R} \left(\frac{p_0}{p_{ref}}\right)^{1/\gamma} \tag{3.40}$$

$$\nabla \cdot (P_0 \mathbf{u}) = S - (P_0)_t. \tag{3.41}$$

Comparing equations (3.32)-(3.41) to the dry pseudo-incompressible model of the previous chapter we can see that as well as the extra equations for the species and the source term in the $P$ equation we also require an equations set which governs the evolution of the background state.

Unlike the model in Almgren et al. (2008) we have not needed to define new horizontally averaged variable in order to calculate our divergence constraint. However, the reason for this is that we have defined $\gamma$ as constant and if a non-constant gamma were required a similar style variable would have to be utilised.

# Chapter 4

# Numerical details

## 4.1 Overview of the numerics

Equation sets (2.18)-(2.20) and (3.32)-(3.41) are solved using a predictor-corrector finite volume code based on the numerical techniques described in Klein (2009) which is composed of two predictor and two corrector steps. The primary variables, $\rho, \rho\mathbf{u}, \rho q_v, \rho q_c$, and $P_0$ are stored at cell centers, whereas the perturbation pressure $p$ is stored at grid nodes. Fluxes of conserved variables arise at grid cell interfaces which is standard for cell-centered finite volume code. A schematic of the grid set-up is given in Figure 4.2.

In the predictor step the variables are advected forward in time to second order but the divergence constraint is ignored and $P$ is advected in the same way as the other primary variables. Also, the old time level pressure is used in the momentum equation since the pressure update is not known until after the corrector step. These two simplifications result in a reduced order of accuracy in the momentum equation due to advective fluxes that do not satisfy the divergence constraint and also due to the usage old time level pressure. For each model, the timestep is calculated according to the Courant–Friedrichs–Lewy (CFL) condition (see LeVeque (2002) and section 4.4) and the pressure is initialised in a well balanced fashion (see section 4.3).

These inaccuracies are corrected in the two corrector steps. The advective fluxes are corrected in the first step and the error in the momentum equation due to the usage of the old time level pressure is corrected in the second step.

To calculate the microphysical source terms we use the method of saturation adjustment outlined in Grabowski and Smolarkiewicz (1990) after the predictor step but before the corrector steps. As in Kurowski et al. (2013) the source term calculation comes in two varieties: one model $\mathrm{PI}_m^{\mathrm{tc},p_0}$ uses $p_0$ in the source term calculation and the other model $\mathrm{PI}_m^{\mathrm{tc},p}$ uses $p$ in the source term calculation.

In the dry case we will also implement a "naive" model which ignores the extra term required by thermodynamic consistency. This model will be denoted as PI. A summary of the model notation used is given in Figure 4.1.

Note, in the current chapter the asterisk will be dropped from the pseudo-density in order to simplify the notation.

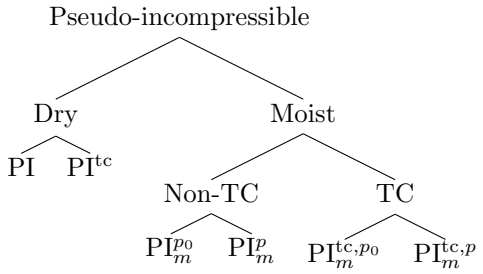


Figure 4.1: Tree of model notation used in the paper where "TC" stands for thermodynamically consistent. The moist "Non-TC" branch corresponds to the model of O'Neill and Klein (2013) and is not implemented in the present work.

## 4.2 Explanation of the numerics notation

The notation used in this section is given as follows

$i$ - Grid cell index in the horizontal direction
$i_{min}$ - Minimum grid cell index in the horizontal direction
$i_{max}$ - Maximum grid cell index in the horizontal direction
$j$ - Grid cell index in the vertical direction
$j_{min}$ - Minimum grid cell index in the vertical direction
$j_{max}$ - Maximum grid cell index in the vertical direction
$x$ - Horizontal position
$z$ - Vertical position
$\Delta t$ - Time step size
$\Delta x$ - Grid cell size in x-direction
$\Delta z$ - Grid cell size in x-direction
$u$ - Horizontal velocity
$w$ - Vertical velocity
$(.)^n$ - Denotes values at the end of previous time step
$(.)^{n+1}$ - Denotes values at the end of current time step
$(.)^{pred}$ - Denotes values at the end of the predictor step
$(.)^{pred}$ - Denotes values at the end of the first projection step
$\alpha$ - Thermodynamically consistent switching parameter
$\beta$ - Moist/Dry switching parameter

Note, any variables that have a $j$ index and no $i$ index do not depend on $x$.

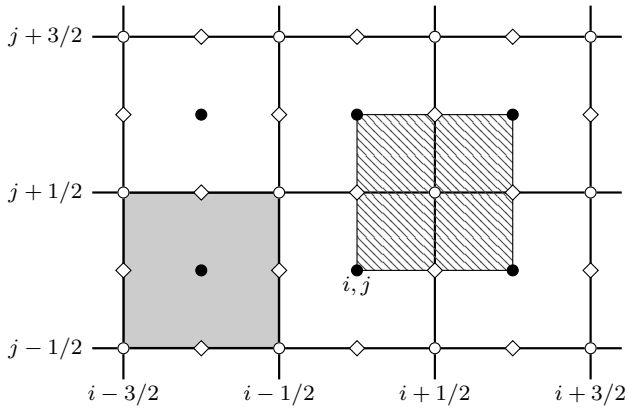


Figure 4.2: Schematic of the computational grid. The filled-in dots are the cell centers, the white dots are the nodes, the diamond shapes are the the cell interfaces, the large shaded square is a primary cell and the large line-filled cell is a dual cell.

## 4.3 Well balancing

Since our model is not written in perturbational form extra care must to taken to ensure that the non-perturbed pressure discretely satisfies the hydrostatic balance. After the primary variables are initialised we calculate the nodal pressure from the cell-centered density by integrating (2.9) up from the bottom to get

$$p_{0j+1/2} = p_{0j-1/2} - \rho_{0j} g \Delta z \tag{4.1}$$

where $p_{0j_{min}-1/2} = p_{ref}$. This ensures that if the the density is initially hydrostatic then the pressure and gravity term will cancel exactly in the momentum equation.

It is also possible not just to initialise hydrostatically but also to implement the predictor step in a well balanced fashion by following the methods of Botta et al. (2004) but in the present work it is only the initialisation which will be well balanced.

## 4.4 Time step calculation

In the dry testcases the timestep is calculated by taking the minimum of the buoyancy timestep $\Delta t_b$ and the advection timestep $\Delta t_{adv}$. These timsteps choices are defined as

$$\Delta t_b = \text{CFL} \max \sqrt{\frac{\Delta x \theta_0}{g(\theta - \theta_0)}} \quad \text{and} \quad \Delta t_{adv} = \text{CFL} \frac{\Delta x}{\max \|\mathbf{u}\|} \tag{4.2}$$

where $0 \leq \text{CFL} \leq 1$ is defined for each testcase independently and the function max returns the maximum cell value in the domain. The final timestep is given as

$$\Delta t = \min(\Delta t_b, \Delta t_{adv}). \tag{4.3}$$

In the moist testcases the buoyancy timestep was found to be an insufficient upper bound and a maximum timestep $\Delta t_{max}$ was defined for each testcase. The final timestep is then calculated by taking the minimum of the maximum timestep $\Delta t_{max}$ and the advection timestep $\Delta t_{adv}$

$$\Delta t = \min(\Delta t_{max}, \Delta t_{adv}). \tag{4.4}$$

## 4.5 The predictor step

In this step the advective updates for $\rho$, $\rho\mathbf{u}$, $P$, $\rho q_v$ and $\rho q_c$ are calculated while ignoring pressure updates, the latent heat term and the condensation source terms. We will make a few modifications from the equations given in the previous chapters. For the numerics we will write the gravity source term in terms of $P_0$ and $\theta_q$ by using the equations of state (2.10) and (3.13) and taking note that in the dry case $\theta_q \equiv \theta$. Although this seems unnecessary, using $P_0$ and $\theta_q$ was found to have much better stability for larger timesteps when compared

with using $\rho$. The reason for this is that using $P_0$ and $\theta$ shields the momentum from the divergence errors accumulated by $\rho$ in the first step of the predictor.

The time integration is preformed using a two step strong stability preserving Runge-Kutta scheme from Gottlieb et al. (2001). These steps can be written in general form as

1. Step One

$$\begin{aligned}\phi^*_{i,j} =&\phi^n_{i,j} + \frac{\Delta t}{\Delta x}\left((\phi u)^n_{i+\frac{1}{2},j} - (\phi u)^n_{i-\frac{1}{2},j}\right)\\ &+ \frac{\Delta t}{\Delta z}\left((\phi w)^n_{i,j+\frac{1}{2}} - (\phi w)^n_{i,j-\frac{1}{2}}\right) - \Delta t Q^\phi_{i,j}\end{aligned} \tag{4.5}$$

2. Step Two

$$\begin{aligned}\phi^{**}_{i,j} =&\frac{1}{2}\left(\phi^n_{i,j} + \phi^*_{i,j}\right) + \frac{\Delta t}{2\Delta x}\left((\phi v)^*_{i+\frac{1}{2},j} - (\phi v)^*_{i-\frac{1}{2},j}\right)\\ &+ \frac{\Delta t}{2\Delta z}\left((\phi w)^*_{i,j+\frac{1}{2}} - (\phi w)^*_{i,j-\frac{1}{2}}\right) - \frac{\Delta t}{2} Q^{\phi,*}_{i,j} g\end{aligned} \tag{4.6}$$

where $\phi \in \{\rho, \rho u, \rho w, P\}$ for the dry models and $\phi \in \{\rho, \rho u, \rho w, P, \rho q_v, \rho q_c\}$ for the moist models. The source term $Q^\phi_{i,j}$ is written as

$$Q^\phi_{i,j} = \begin{cases} 0 & (\phi \in \{\rho, P, \rho q_v, \rho q_c\}) \\ \frac{1}{\Delta x}\left(p^n_{i+\frac{1}{2},j} - p^n_{i-\frac{1}{2},j}\right) & (\phi \in \{\rho u\}) \\ \frac{1}{\Delta z}\left(p^n_{i,j+\frac{1}{2}} - p^n_{i,j-\frac{1}{2}}\right) + \left(\frac{P}{\theta_q} + \alpha\frac{\rho_0}{\gamma p_0}p'\right)^n_{i,j} & (\phi \in \{\rho w\}) \end{cases} \tag{4.7}$$

where $Q^{\phi,*}_{i,j}$ in (4.6) indicates that $\theta^*_{q\,i,j} = P^*_{i,j}/\rho^*_{i,j}$ is to be used in the gravity term but the remaining terms are at time level $n$ and $\alpha$ is a switching parameter such that

$$\alpha = \begin{cases} 0 & \text{PI} \\ 1 & \text{PI}^{\text{tc}},\ \text{PI}^{\text{tc},p}_m,\ \text{PI}^{\text{tc},p_0}_m \end{cases}. \tag{4.8}$$

The fluxes in this step are calculated as follows, the velocities on the cell faces are determined using

$$u = \frac{1}{2}\left(u_L + u_R\right) \tag{4.9}$$

$$w = \frac{1}{2}\left(w_L + w_R\right) \tag{4.10}$$

where the $L$ and $R$ subscripts signify reconstructed values on the left and right of the interface. These values are reconstructed using a prescribed limiter. Then, the fluxes are calculated in an upwind fashion, for example, to calculate $(\phi u)^n_{i+\frac{1}{2},j}$ we let

$$(\phi u)^n_{i+\frac{1}{2},j} = \left((\phi u)^n_{i+\frac{1}{2},j}\right)^+ + \left((\phi u)^n_{i+\frac{1}{2},j}\right)^- \tag{4.11}$$

where

$$\left((\phi u)^n_{i+\frac{1}{2},j}\right)^+ = \left(\phi^n_{i+\frac{1}{2},j}\right)_L * \max(0,u) \tag{4.12}$$

and

$$\left((\phi u)^n_{i+\frac{1}{2},j}\right)^- = \left(\phi^n_{i+\frac{1}{2},j}\right)_R * \min(0,u). \tag{4.13}$$

The remaining fluxes can be calculated using the same method.

## 4.6 Microphysics step

In this step we calculate the microphysical source terms and use them to update $\rho q_v$, $\rho q_c$ and $P$. Following Grabowski and Smolarkiewicz (1990) the condensation rate in a single cell over one time-step can be calculated using

$$C^n_{i,j} = \left[\frac{(q^{**}_v - q^{**}_{vs})}{\left(1 + (1+q^{**}_{vs}/\epsilon)\left(\frac{q^{**}_{vs}L^n_v}{c_p}\frac{L_{v0}}{R_v T^{**2}}\right)\right)\Delta t}\right]_{i,j} \tag{4.14}$$

where $q_{vs}$ is the vapour saturation mixing ratio and

$$T^{**} = \begin{cases} \theta^{**}(p^n_0/p_{ref})^{(R/c_p)}, & \mathrm{PI}^{\mathrm{tc},p_0}_m \\ \theta^{**}(p^n/p_{ref})^{(R/c_p)}, & \mathrm{PI}^{\mathrm{tc},p}_m \end{cases} \tag{4.15}$$

where $q^{**}_v = [(\rho q_v)/\rho]^{**}$ and $\theta^{**}_q = \left[\left(\frac{1+q}{1+q_v/\epsilon}\right)P/\rho\right]^{**}$. The vapour saturation mixing ratio can be calculated following Lipps and Helmer (1982) using

$$q_{vs} = \frac{\epsilon e_s}{p_0 - e_s} \tag{4.16}$$

where the saturation vapour pressure is given by the

$$e_s = e_0 \exp\left(\frac{L_{v0}}{R_v}\left(\frac{1}{T_{ref}} - \frac{1}{T}\right)\right) \tag{4.17}$$

with $e_0 = 611.0$ Pa.

Using $C_{i,j}$ we can now calculate the latent heat rate over one time-step as

$$S^n_{i,j} = \left[\left(\frac{L_v}{c_p T}\right) - 1/(\epsilon + q_v)\right]^n_{i,j} P^n_{i,j} C^n_{i,j}. \tag{4.18}$$

Finally, the microphysical updates are given as

$$(\rho q_v)^{pred}_{i,j} = (\rho q_v)^{**}_{i,j} - C^n_{i,j}\Delta t \tag{4.19}$$

$$(\rho q_c)^{pred}_{i,j} = (\rho q_v)^{**}_{i,j} + C^n_{i,j}\Delta t \tag{4.20}$$

$$P^{pred}_{i,j} = P^{**}_{i,j} + S^n_{i,j}\Delta t \tag{4.21}$$

The variables $\rho^{**}$, $(\rho u)^{**}$ and $(\rho w)^{**}$ will also be written with a "*pred*" superscript since they also contain the predicted values.

## 4.7 Background state update

To calculate the background state at the new time level we must first calculate the rate of change of $p_0^{top}$ over the current time-step using (3.38). This is done as follows

$$\left(\frac{\partial p_0^{top}}{\partial t}\right)^n = \frac{\sum_{j=j_{min}}^{j_{max}} (AVG(S)/P_0)_j^n}{\sum_{j=j_{min}}^{j_{max}} (1/\gamma p_0)_j^n} \tag{4.22}$$

where $AVG$ is the discrete approximation of the horizontal average and is given by $AVG(\cdot) = \frac{1}{(i_{max}-i_{min})} \sum_{i=i_{min}}^{i_{max}} (\cdot)$. We then use the value calculated from (4.22) to calculate the background velocity on the interface from (3.39) using

$$w_0{}_{j+\frac{1}{2}}^n = \Delta z \left[ \sum_{k=j_{min}}^{j} \left( (AVG(S)/P_0)_k^n - (1/\gamma p_0)_k^n \left( \frac{\partial p_0^{top}}{\partial t} \right)^n \right) \right] \tag{4.23}$$

The updates of $\rho_0$ and $P_0$ are then calculated from (3.36) and (3.37) using

$$(\rho_0)_j^{n+1} = (\rho_0)_j^n + \frac{\Delta t}{\Delta z} \left( (\rho_0 w_0)_{j+1/2}^n - (\rho_0 w_0)_{j-1/2}^n \right) \tag{4.24}$$

$$(P_0)_j^{n+1} = (P_0)_j^n + \frac{\Delta t}{\Delta z} \left( (P_0 w_0)_{j+1/2}^n - (P_0 w_0)_{j-1/2}^n \right) + AVG(S)_j^n \Delta t. \tag{4.25}$$

Finally, we need to update the background values in the momentum equation in the $\mathrm{PI}_m^{\mathrm{tc},p_0}$ and $\mathrm{PI}_m^{\mathrm{tc},p}$ models. This is done using the following equation

$$(\rho w)_{i,j}^{pred} = (\rho w)_{i,j}^{**} + \frac{\Delta t}{2} \left[ \left( \frac{\rho_0}{\gamma p_0} \right)_j^{n+1} (p^n - p_0^{n+1})_j - \left( \frac{\rho_0}{\gamma p_0} \right)_j^{n} (p^n - p_0^n)_j \right]. \tag{4.26}$$

After applying (4.26) the background values in the momentum equation are now at the correct half time level and the gravity term will now have the form $\left(\frac{\rho_0}{\gamma p_0}\right)^{n+1/2} \left(p^n - p_0^{n+1/2}\right)$ with $p$ remaining at time level $n$.

## 4.8 First projection

In this step the advective fluxes are corrected to satisfy the divergence constraints given by (2.20) and (3.41). From Klein (2009) we write a Poisson equation which can be used to determine a cell centered pressure correction $\partial p_c$. The gradient of this pressure correction is used to correct the fluxes in the $P$ equation as follows

$$\nabla \cdot (P\mathbf{u})_{i,j}^{n+1} = \nabla \cdot (P\mathbf{u})_{i,j}^{pred} - \Delta t \left( \nabla \cdot \frac{P^{pred}}{\rho^{pred}} (\nabla \partial p_c) \right)_{i,j}. \tag{4.27}$$

Since the terms at $n+1$ satisfy the divergence constraint we re-write (4.27) as

$$\beta\left(S_{i,j}^{n}-\left(\frac{P_0^{n+1}-P_0^{n}}{\Delta t}\right)_j\right)=\nabla\cdot(P\mathbf{u})_{i,j}^{pred}-\Delta t\left(\nabla\cdot\frac{P^{pred}}{\rho^{pred}}\left(\nabla\partial p_c\right)\right)_{i,j}. \tag{4.28}$$

where

$$\beta=\begin{cases}0, & \text{PI, PI}^{\text{tc}}\\ 1, & \text{PI}_m^{\text{tc},p_0}\text{, PI}_m^{\text{tc},p}\end{cases} \tag{4.29}$$

switches between the dry and moist cases. Now using the fact that $\nabla\cdot(P\mathbf{u})_{i,j}^{pred}-\beta S_{i,j}^{n}=-\left(\frac{P^{pred}-P^{n}}{\Delta t}\right)_{i,j}$ due to the predictor step we get

$$\left(\frac{P^{pred}-P^{n}}{\Delta t}\right)_{i,j}-\beta\left(\frac{P_0^{n+1}-P_0^{n}}{\Delta t}\right)_j=-\Delta t\left(\nabla\cdot\frac{P^{pred}}{\rho^{pred}}\left(\nabla\partial p_c\right)\right)_{i,j}. \tag{4.30}$$

We then solve this Poisson equation using subroutines from the HYPRE package (see Falgout and Yang (2002)). After solving for $\partial p_c$ we write the flux update to the $P$ equation as

$$(\partial(P\mathbf{u})\cdot\mathbf{n})_{i,j}=\left(\Delta t\frac{P^{pred}}{\rho^{pred}}\left(\nabla\partial p_c\right)\cdot\mathbf{n}\right)_{i,j} \tag{4.31}$$

and then the advected variables are updated as follows

$$\begin{aligned}\phi_{i,j}^{firstPro}=&\phi_{i,j}^{pred}+\frac{\Delta t}{\Delta x}\left(\left(\partial(Pu)\frac{\phi^{pred}}{P^{pred}}\right)_{i+\frac{1}{2},j}-\left(\partial(Pu)\frac{\phi^{pred}}{P^{pred}}\right)_{i-\frac{1}{2},j}\right)\\&+\frac{\Delta t}{\Delta z}\left(\left(\partial(Pw)\frac{\phi^{pred}}{P^{pred}}\right)_{i,j+\frac{1}{2}}-\left(\partial(Pw)\frac{\phi^{pred}}{P^{pred}}\right)_{i,j-\frac{1}{2}}\right).\end{aligned} \tag{4.32}$$

For $\phi=\rho,\rho u,\rho w,P,\rho q_v,\rho q_c$ the values are now the fully corrected values since their evolution equations do not contain pressure however, for $\phi=\rho u,\rho w$ the pressure remains to be corrected and that is carried out in the second projection.

## 4.9 Second projection

In this final step the cell-centered momenta are corrected by an increment of the nodal pressure in order to bring the pressure in the momentum to the correct half time level. This pressure increment is determined again through a Poisson equation that is derived from the divergence constraint given by (2.20) and (3.41). Integrating the momentum equation to second order accuracy over one

time-step

$$
\begin{aligned}
(\rho\mathbf{u})^{(n+1)} &= (\rho\mathbf{u})^{(n)} - \Delta t \left( \nabla \cdot (\rho\mathbf{u} \circ \mathbf{u}) + \nabla p + g\mathbf{k} \left( \frac{P}{\theta_q} + \alpha \frac{\rho_0}{\gamma p_0}(p - p_0) \right) \right)^{(n+\frac{1}{2})} \\
&= (\rho\mathbf{u})^{(n)} - \Delta t \left( \nabla \cdot (\rho\mathbf{u} \circ \mathbf{u}) + g\mathbf{k} \frac{P}{\theta_q} \right)^{(n+\frac{1}{2})} - \nabla \left( \frac{p^{n+1} + p^n}{2} \right) \\
&\quad - \alpha g\mathbf{k} \left( \frac{\rho_0}{\gamma p_0} \right)^{n+\frac{1}{2}} \left[ \frac{(p^{n+1} - p_0^{n+1}) + (p^n - p_0^n)}{2} \right] \\
&= (\rho\mathbf{u})^{(n)} - \Delta t \left( \nabla \cdot (\rho\mathbf{u} \circ \mathbf{u}) + g\mathbf{k} \frac{P}{\theta_q} \right)^{(n+\frac{1}{2})} - \nabla p^n \\
&\quad - \alpha g\mathbf{k} \left( \frac{\rho_0}{\gamma p_0} \right)^{n+\frac{1}{2}} \left[ \frac{(p^n - p_0^{n+1}) + (p^n - p_0^n)}{2} \right] \\
&\quad + \nabla \left( \frac{p^{n+1} - p^n}{2} \right) - \alpha g\mathbf{k} \left( \frac{\rho_0}{\gamma p_0} \right)^{n+\frac{1}{2}} \frac{p^{n+1} - p^n}{2} \\
&= (\rho\mathbf{u})^{(n+1, firstPro)} - \nabla \left( \frac{p^{n+1} - p^n}{2} \right) - \alpha g\mathbf{k} \left( \frac{\rho_0}{\gamma p_0} \right)^{n+\frac{1}{2}} \frac{p^{n+1} - p^n}{2} \\
&= (\rho\mathbf{u})^{(n+1, firstPro)} - \Delta t \left( \nabla \delta p_N + \alpha \left( \frac{\rho_0 g}{\gamma p_0} \right)^{(n+\frac{1}{2})} \delta p \mathbf{k} \right) \qquad (4.33)
\end{aligned}
$$

where we define

$$
\delta p_N = \frac{p^{n+1} - p^n}{2}. \qquad (4.34)
$$

Multiplying (4.33) by $\theta_q^{n+1}$

$$
(P\mathbf{u})^{(n+1)} = (P\mathbf{u})^{(n+1, firstPro)} - \Delta t \left( \frac{P}{\rho} \right)^{n+1} \left( \nabla \delta p_N + \alpha \left( \frac{\rho_0 g}{\gamma p_0} \right)^{(n+\frac{1}{2})} \delta p_N \mathbf{k} \right) \qquad (4.35)
$$

and then taking the divergence of (4.35) and re-arranging we get

$$
\begin{aligned}
\frac{\Delta t}{2} \nabla \cdot \left[ \left( \frac{P}{\rho} \right)^{n+1} \left( \nabla \partial p_N + \alpha \left( \frac{\rho_0 g}{\gamma p_0} \right)^{(n+\frac{1}{2})} \delta p_N \mathbf{k} \right) \right] &= \nabla \cdot (P\mathbf{u})^{firstPro} \\
&\quad - \beta \left( S^n - \frac{{P_0}^{n+1} - {P_0}^n}{\Delta t} \right). \qquad (4.36)
\end{aligned}
$$

After solving for $\partial p_N$ on the dual cells the velocity is updated using

$$
\begin{aligned}
(\rho u)_{i,j}^{n+1} = &(\rho u)_{i,j}^{firstPro} - \frac{\Delta t}{2\Delta x} \Big( (\partial p_{N\, i+\frac{1}{2}, j+\frac{1}{2}} + \partial p_{N\, i+\frac{1}{2}, j-\frac{1}{2}}) \qquad (4.37) \\
&- (\partial p_{N\, i-\frac{1}{2}, j+\frac{1}{2}} + \partial p_{N\, i-\frac{1}{2}, j-\frac{1}{2}}) \Big) \qquad (4.38)
\end{aligned}
$$

and

$$(\rho w)_{i,j}^{n+1} = (\rho w)_{i,j}^{firstPro} - \frac{\Delta t}{2\Delta z}\Big((\partial p_{N\,i+\frac{1}{2},j+\frac{1}{2}} + \partial p_{N\,i-\frac{1}{2},j+\frac{1}{2}}) \tag{4.39}$$

$$-(\partial p_{N\,i+\frac{1}{2},j-\frac{1}{2}} + \partial p_{N\,i-\frac{1}{2},j-\frac{1}{2}})\Big) - \Delta t\alpha\left(\frac{\rho_0 g}{p_0\gamma}\right)^{n+\frac{1}{2}}\partial p' \tag{4.40}$$

and the pressure is updated using (4.34)

$$p^{n+1} = p^n + 2\delta p' \tag{4.41}$$

where $\partial p' = \Big(\partial p_{N\,i+\frac{1}{2},j-\frac{1}{2}} + \partial p_{N\,i+\frac{1}{2},j+\frac{1}{2}} + \partial p_{N\,i-\frac{1}{2},j-\frac{1}{2}} + \partial p_{N\,i-\frac{1}{2},j+\frac{1}{2}}\Big)/4$.

Now the pressure and the primary variables are second order accurate at the new time level and they also satisfy the divergence constraint.

# Chapter 5

# Numerical results

## 5.1 Overview of the numerical results

In this section the performance of both the dry and moist models are examined in a number of idealised testcases. The testcases are composed of both warm and cold perturbations applied to a hydrostatic background state. The model results are compared with published results of both anelastic and compressible models. In the dry cases, the constants $R$ and $\gamma$ are equal to 287 $\mathrm{N\,m\,kg^{-1}\,K^{-1}}$ and 1.4 respectively. In the moist cases the thermodynamic constants vary and the values for each testcase can be found in Appendix B.

## 5.2 Dry testcases

The aim of the dry testcases is two-fold, we wish to test the importance of the extra buoyancy term required by thermodynamic consistency and we wish to judge how our model compares against the reference models. To test the former we will be running all the dry testcases with both the PI and $\mathrm{PI^{tc}}$ models and to test the latter we will compare our results with the ones given in the reference papers.

### 5.2.1 Dry rising bubble

The dry rising bubble testcase consists of an initially neutrally stratified atmosphere at rest with a warm bubble perturbation placed near the bottom of the domain. The domain is 20km wide and 10km high with solid-wall vertical boundary conditions and periodic horizontal boundary conditions. The hydrostatic background values are defined as in Klein (2009) and are evaluated using

$$\begin{aligned} \theta_0 &= T_{ref} \\ p_0 &= p_{ref}\left(1 - \frac{\gamma-1}{\gamma}\frac{zg}{RT_{ref}}\right)^{\frac{\gamma}{\gamma-1}} \\ \rho_0 &= \frac{p_{ref}}{\theta_0 R}\left(1 - \frac{\gamma-1}{\gamma}\frac{zg}{RT_{ref}}\right)^{\frac{1}{\gamma-1}} \end{aligned} \tag{5.1}$$

where $T_{ref} = 300$ K, $p_{ref} = 8.61 \times 10^4$ Pa and $g = 10\ \mathrm{m\,s^{-2}}$.

After initialising with the hydrostatic values a perturbation is added to the density and potential temperature. The perturbed values are defined as in Klein (2009) and are calculated using

$$\left.\begin{aligned} \theta &= \theta_0 + d\theta\cos^2\left(\frac{\pi}{2}r\right) \\ \rho &= \frac{p_{ref}}{\theta R}\left(1 - \frac{\gamma-1}{\gamma}\frac{zg}{RT_{ref}}\right)^{\frac{1}{\gamma-1}} \end{aligned}\right\} \text{ for } r \leq 1 \tag{5.2}$$

where $d\theta = 2$ K, $r = 5\sqrt{(x/L)^2 + (z/L - 1/5)^2}$ and $L = 10$ km. A contour plot of the initial potential temperature can be seen in Figure 5.1.

The warm bubble is more buoyant than the surrounding air and, as expected, it rises through the domain during the simulation. The simulation is run until $t = 1000$ s and the solutions are then examined. The calculations are preformed with CFL = 0.5 and a constant grid size in the vertical and horizontal of 125 m.

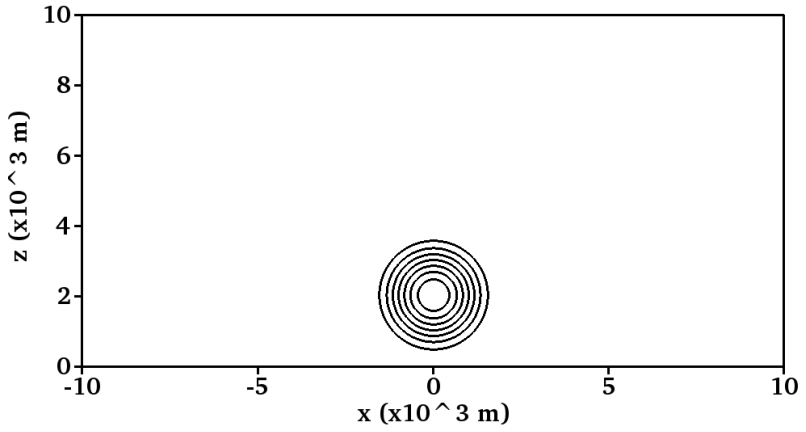


Figure 5.1: A contour plot of the initial potential temperature perturbation at $t = 0$ s for the dry rising bubble testcase where the contour interval is 0.25 K.

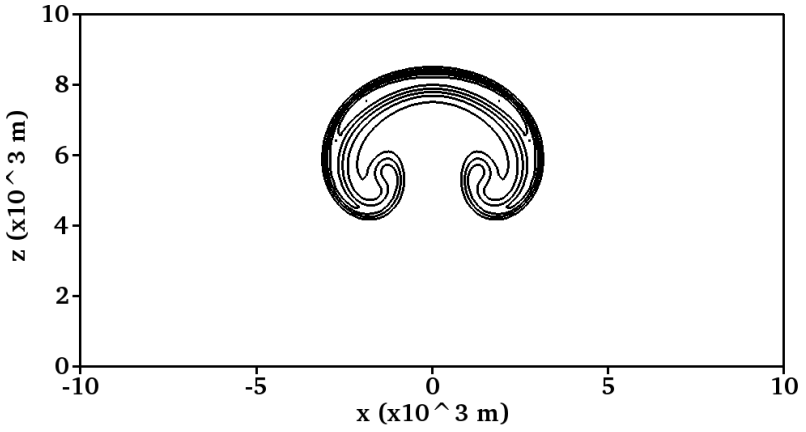


Figure 5.2: A contour plot of the perturbation of the potential temperature at $t = 1000$ s for the dry rising bubble testcase using the PI model where the contour interval is 0.25 K.

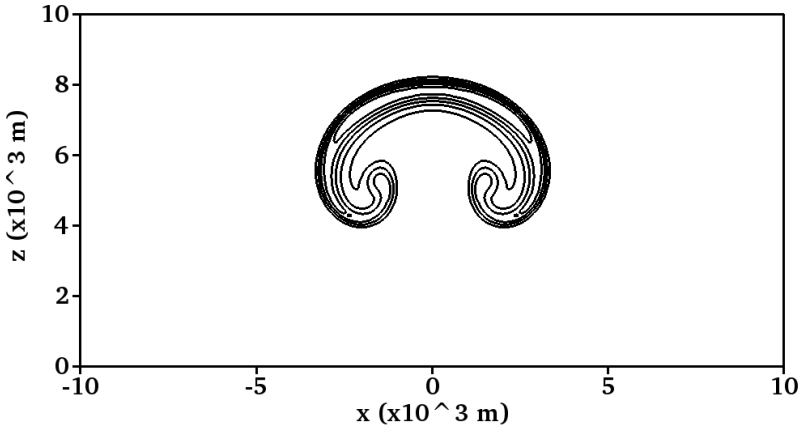


Figure 5.3: A contour plot of the perturbation of the potential temperature at $t = 1000$ s for the dry bubble testcase using the $\mathrm{PI}^{\mathrm{tc}}$ model where the contour interval is 0.25 K.

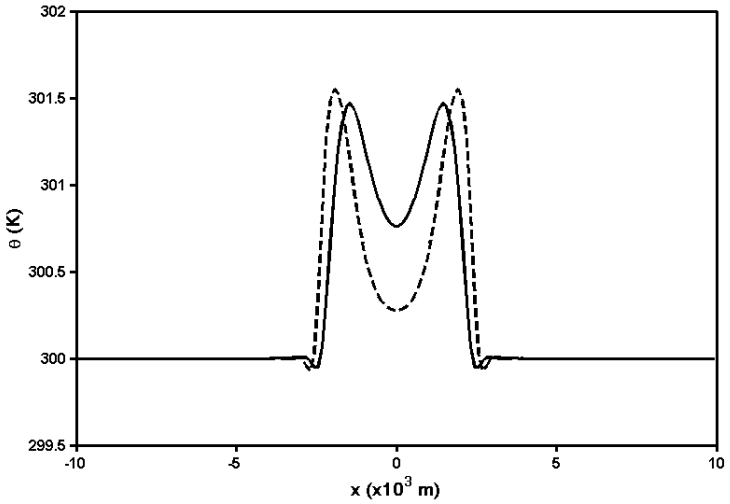


Figure 5.4: Horizontal cut at height 7500 m of the potential temperature in the dry rising bubble testcase at final time $t = 1000$ s for the $\mathrm{PI}^{\mathrm{tc}}$ model (solid) and the PI model (dashed).

| | $\theta'_{\max}$ | $z_{\text{front}}$ | $x_{\text{right}} - x_{\text{left}}$ |
|---|---|---|---|
| REF | 1.73 K | $\approx$ 8200.0 m | $\approx$ 6600.0 m |
| PI$^{\text{tc}}$ | 1.53 K | 8187.34 m | 6647.66 m |
| PI | 1.54 K | 8469.32 m | 6278.38 m |

Table 5.1: Maximum temperature perturbation $\theta'_{\max}$, height $z_{\text{front}}$, and horizontal extension $x_{\text{right}} - x_{\text{left}}$ at final time $t = 1000$ s for the reference model in Klein (2009) (REF) and the PI$^{\text{tc}}$ and PI models for the dry rising bubble testcase.

Comparing the results at the final time $t = 1000$s for the PI and PI$^{\text{tc}}$ models in Fig. 5.2, Fig. 5.3 and Table 5.1 one can see that the PI bubble rises higher than the PI$^{\text{tc}}$ bubble and also its tails are closer together. These differences are caused by a phase shift between the models and can be clearly seen in the cut plot in Figure 5.4. Comparing the models to the reference values in Klein (2009) in Table 5.4 we find that the TC bubble height and width at the final time is a much better fit but our models do a worse job at conserving the potential temperature perturbation due to, most likely, higher numerical diffusion for our scheme.

The discrepancies in the PI model come from neglecting the effect of pressure perturbations on the buoyancy. The extra buoyancy term present in the PI$^{\text{tc}}$ model reduces buoyancy near the top of the bubble due to an increase in pressure near the bubble top and increases buoyancy at the two tails due to a pressure decrease near the tails. Furthermore, the overall buoyancy of the bubble decreases causing a decrease in the phase speed. Therefore the PI$^{\text{tc}}$ bubble is both lower and wider than the PI model and, as a result, the PI$^{\text{tc}}$ results resembles the reference model results more closely.

### 5.2.2 Density current

In the density current testcase the hydrostatic values are initialised with (5.1) as in the rising bubble testcase except this time $p_{ref} = 10 \times 10^4$ Pa, $g = 9.81\ \text{m s}^{-2}$ and this time we will apply a negative perturbation. The domain is 51.2km wide and 6.4km high with solid-wall vertical boundary conditions and periodic horizontal boundary conditions. We use the same perturbation defined in Straka et al. (1993) which is given by

$$dT = -15(1 + \cos(\pi r))/2 \text{ K for } r \leq 1 \tag{5.3}$$

where $r = \sqrt{(x/2L)^2 + ((z - z_c)/L)^2}$, $L = 2$ km and $z_c = 3$ km. The potential temperature perturbation and the density perturbation are then calculated using (2.4) and (2.5). A plot of the initial potential temperature perturbation is presented in Figure 5.5. The calculations are preformed with CFL = 0.5 and a constant grid size in the vertical and horizontal of 50 m. In addition, an artificial diffusion term given by $\rho\mu\nabla^2\mathbf{u}$ is added to the momentum equation (2.19) (and $\rho\mu\nabla^2\theta$ is added to the P equation) with $\mu = 75\text{m}^2\,\text{s}$ as in Straka et al. (1993).

The cold bubble is less buoyant than the surrounding air and it falls through the domain during the simulation. Once it hits the bottom boundary the moment of the bubble caries along the bottom of the domain on both the left and right directions.

The progression of the PI and PI$^{tc}$ runs at $t = 300$s, 600s and 900s are given in Figure 5.7 and Figure 5.8 respectively. The plots are nearly indistinguishable and it is only when the we examine the variable values in Table 5.2 and the plots in Figure 5.6 that differences can be seen. In contrast to the rising bubble case, the extra buoyancy term in the PI$^{tc}$ model results in an overall increase in the buoyancy of the bubble. This means that the bubble falls slower in the PI$^{tc}$ case and, as a result, does not travel as far as the PI bubble. Although it is not obvious from Table 5.2 which model performs better in the work presented in Benacchio et al. (2014) PI$^{tc}$ was shown to perform much better than PI when compared with a compressible model which utilises the same numerics as the PI$^{tc}$ model.

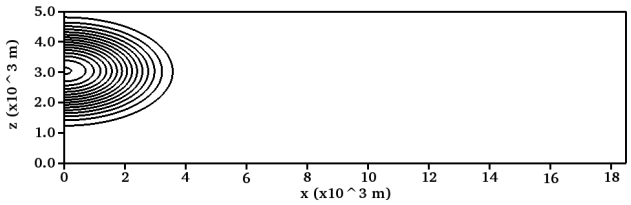


Figure 5.5: A contour plot of the initial potential temperature perturbation in the density current testcase where the contour interval is 1 K.

| | $\theta'_{\max}$ | $x_{\text{front}}$ |
|---|---|---|
| REF | -9.77 K | 15537.44 m |
| PI$^{tc}$ | -9.98 K | 15455.57 m |
| PI | -9.80 K | 15675.83 m |

Table 5.2: Maximum temperature perturbation $\theta'_{\max}$ and front position $x_{\text{front}}$ at the final time $T = 900$ s for the density current testcase. Where $x_{\text{front}}$ is the rightmost intersection of the 1 K contour with the bottom boundary

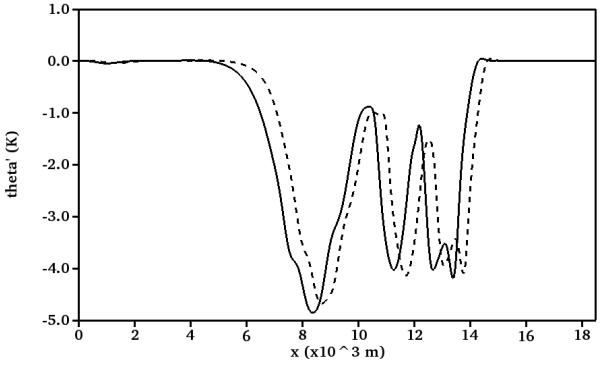


Figure 5.6: Horizontal cut at height 1200 m of the potential temperature perturbation in the density current testcase at final time $t = 900$ s for the PI$^{tc}$ model (solid) and the PI model (dashed).

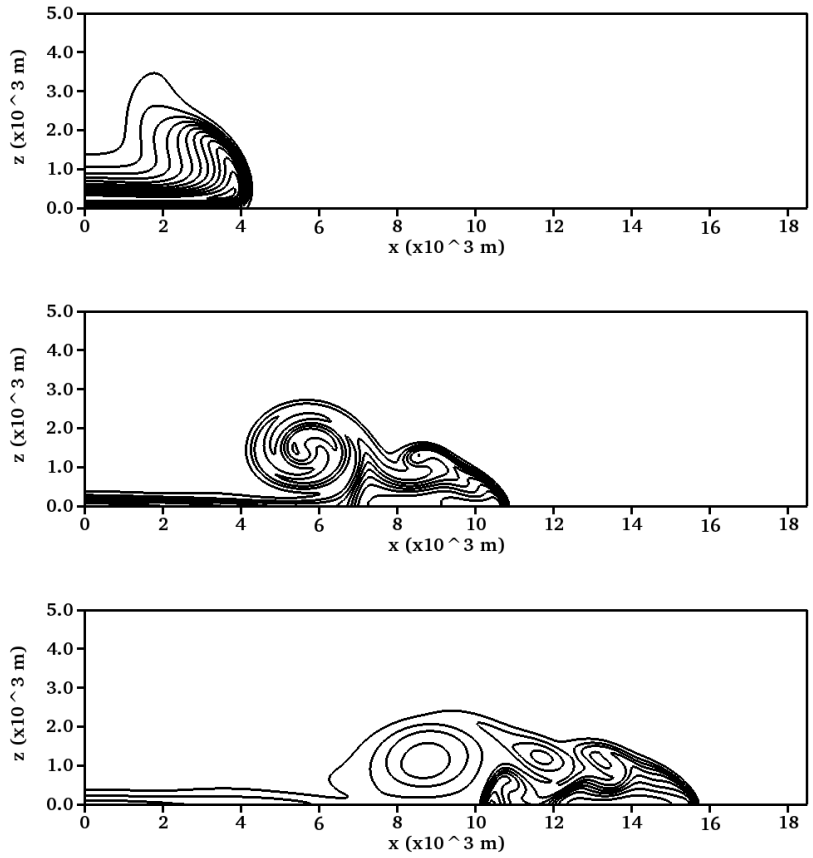


Figure 5.7: Contour plots of the potential temperature perturbation in the density current testcase for the PI model at $t = 300$ s (upper), $t = 600$ s (middle) and $t = 900$ s (bottom) where the contour interval is 1 K .

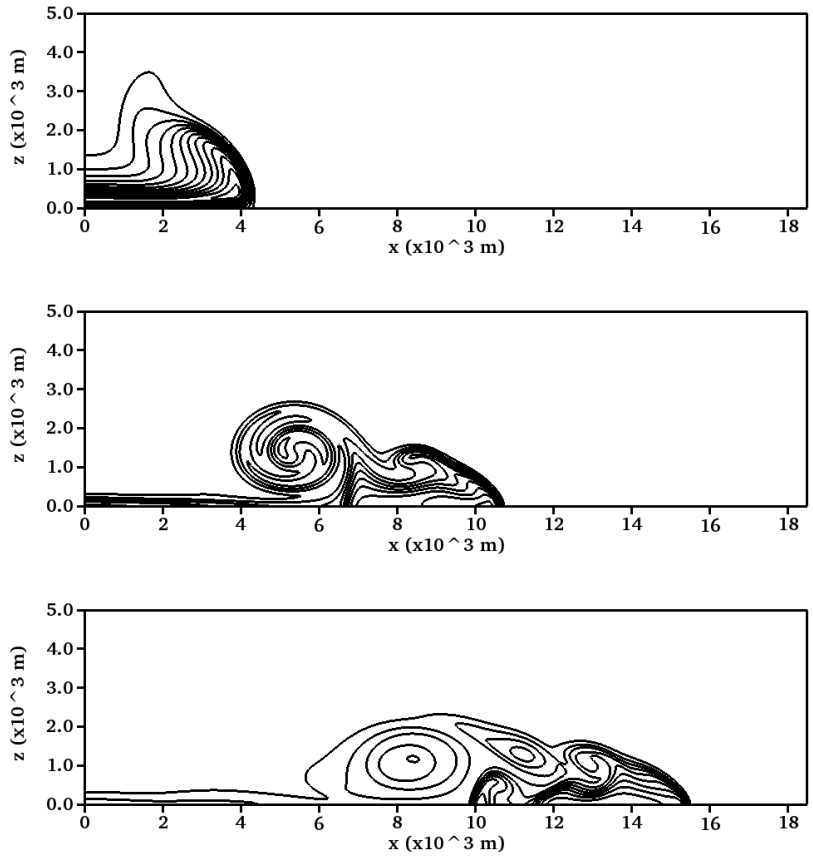


Figure 5.8: Contour plots of the potential temperature perturbation in the density current testcase for the $\mathrm{PI}^{\mathrm{tc}}$ model at $t = 300$ s (upper), $t = 600$ s (middle) and $t = 900$ s (bottom) where the contour interval is 1 K.

### 5.2.3 Inertia gravity wave

As outlined in Skamarock and Klemp (1994) the inertia gravity wave testcase consists of a stably stratified atmosphere with a vertically varying potential temperature and a constant horizontal velocity. The domain is 30 km wide and 10 km high with periodic horizontal boundaries and solid wall upper and lower boundaries. The potential temperature stratification is given by

$$\frac{\partial \theta_0}{\partial z} = \frac{N^2}{g} \tag{5.4}$$

where $N = 0.01\ \mathrm{s}^{-1}$ is the Brunt–Väisälä frequency and $g = 9.81\ \mathrm{m\,s}^{-2}$. Integrating (5.4) in the vertical direction we get the initial condition for hydrostatic potential temperature

$$\theta_0 = \theta_{gnd} \exp\left(\frac{N^2}{g} z\right) \tag{5.5}$$

where $\theta_{gnd} = 288.15$ K is the value at the bottom boundary. Using (5.5) and (2.9) the initial hydrostatic density and pressure can be defined as

$$p_0 = p_{ref}\left[1 - \frac{g}{c_p\theta_0 S}(1 - \exp(-Sz))\right]^{\frac{\gamma}{\gamma-1}} \tag{5.6}$$

$$\rho_0 = \frac{p_{ref}}{\theta_0 R}\left[1 - \frac{g}{c_p\theta_0 S}(1 - \exp(-Sz))\right]^{\frac{1}{\gamma-1}} \tag{5.7}$$

where $p_{ref} = 8.61 \times 10^4$. A perturbation outlined in Skamarock and Klemp (1994) is applied and is given by the equation

$$\theta = \theta_0 + d\theta \sin(\pi z/H) \tag{5.8}$$

where $d\theta = 0.01/(1 + (x - x_c)/a^2)$, $x_c = 100$ km, $a = 5$ km and $H = 10$ km. A contour plot of the initial potential temperature perturbation can be seen in in Figure 5.9. A constant horizontal velocity of 20 $\mathrm{m\,s^{-1}}$ and a zero vertical velocity were applied and the simulations are run with CFL = 0.3 and a constant 250 m grid spacing in both the horizontal and vertical directions. During the running of the testcase the potential temperature perturbation propagates in a wave-like manner in both the positive and negative x-directions and the results are examined at the final time $t = 3000$s.

Conversely to the previous two testcases this testcase is wave rather than buoyancy driven and, as a result, there is less of a variation between the $\mathrm{PI^{tc}}$ and PI models as seen from Figure 5.10 and Figure 5.11. However, differences can be seen when we compare the maximum and minimum of the model variables as shown in Table 5.3. Comparing these values to the reference results from Restelli and Giraldo (2009) we can see that the $\mathrm{PI^{tc}}$ has a much better agreement. Also, both the $\mathrm{PI^{tc}}$ and PI models show better conservation properties than the reference model shown in Table 5.4 however this is most likely a result of a difference in numerical schemes.

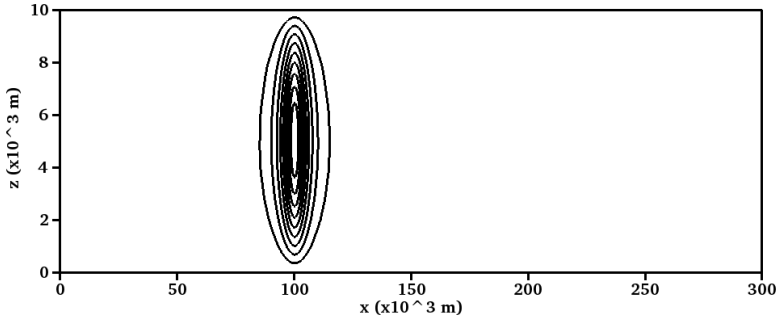


Figure 5.9: A contour plot of the initial potential temperature perturbation for the inertia gravity wave testcase where the contour interval is $10^{-3}$ K.

| | $u'_{\max}$ | $u'_{\min}$ | $w'_{\max}$ | $w'_{\min}$ | $\theta'_{\max}$ | $\theta'_{\min}$ | $\pi'_{\max}$ | $\pi'_{\min}$ |
|---|---|---|---|---|---|---|---|---|
| REF | 1.064E-2 | -1.061E-2 | 2.877E-3 | -2.4E-3 | 2.808E-3 | -1.511E-3 | 9.11E-7 | -7.13E-7 |
| PI$^{\text{tc}}$ | 1.063E-2 | -1.063E-2 | 2.645E-3 | -2.424E-3 | 2.808E-3 | -1.526E-3 | 1.180E-6 | -6.557E-7 |
| PI | 1.365E-2 | -1.362E-2 | 2.763E-3 | -2.471E-3 | 2.930E-3 | -1.709E-3 | 1.210E-6 | -5.36E-7 |

Table 5.3: Table of maxima and minima of horizontal velocity perturbations, vertical velocity, potential temperature and Exner pressure at final time $t = 3000$ s for models PI$^{\text{tc}}$, PI and the reference values from Restelli and Giraldo (2009) (denoted with REF) for the inertia-gravity waves testcase.

| | $C_\rho$ | $C_{\rho u}$ | $C_P$ | $C_{\rho E}$ |
|---|---|---|---|---|
| PI$^{\text{tc}}$ | 6.77E-10 | 9.66E-10 | \ | 3.99E-09 |
| PI | 8.90E-10 | 8.55E-10 | \ | 4.21E-09 |
| REF | 1.67E-08 | 2.6E-07 | \ | 1.64E-08 |

Table 5.4: Table of conservation errors in the inertia gravity waves testcase for density, horizontal momentum density, $P$ and total energy density for the PI$^{\text{tc}}$ and PI models and the reference values (REF) in Restelli and Giraldo (2009).

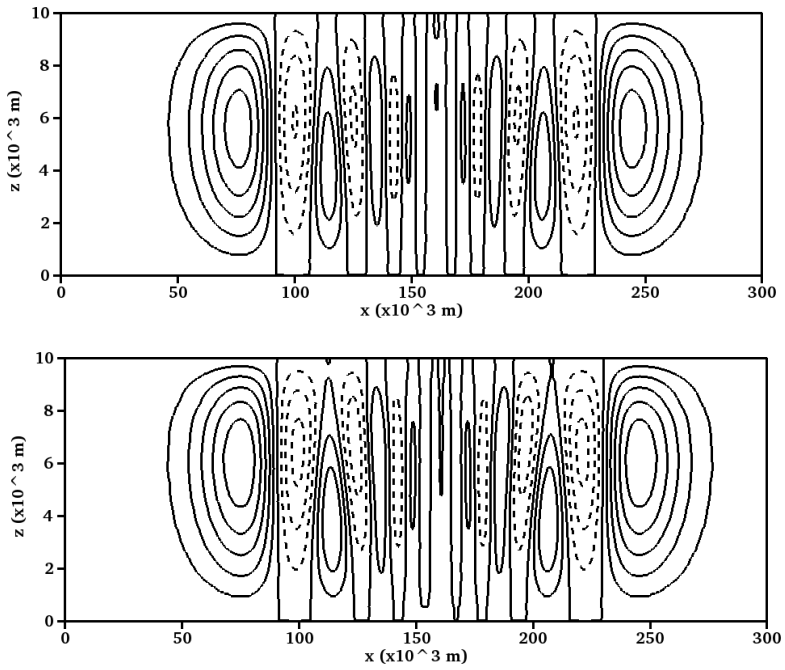


Figure 5.10: Contour plots of the potential temperature perturbation at $t = 3000$ s for the inertia gravity wave testcase for the PI$^{\text{tc}}$ model (top) and the PI model (bottom) where the contour interval is $5 \times 10^{-4}$ K.

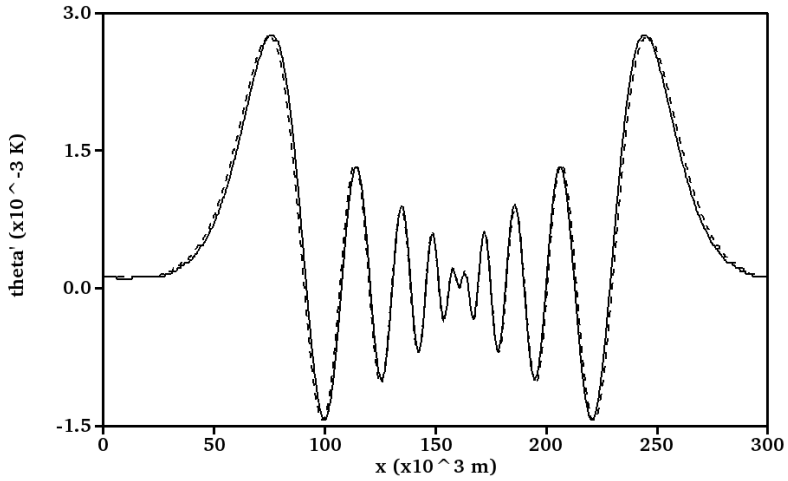


Figure 5.11: Horizontal cut at height 1200 m of the potential temperature perturbation in the inertia gravity waves testcase at final time $t = 900$ s for the $\mathrm{PI}^{\mathrm{tc}}$ model (solid) and the PI model (dashed).

## 5.3 Moist testcases

In the first of the moist testcases we will examine how our the $\mathrm{PI}_m^{\mathrm{tc},p_0}$ model performs against a compressible reference model in a standard benchmark testcase. Whereas, in the second moist testcase we will investigate the effect of the pressure choice in the microphysics by comparing the $\mathrm{PI}_m^{\mathrm{tc},p_0}$ and $\mathrm{PI}_m^{\mathrm{tc},p}$ models.

### 5.3.1 Moist bubble

To test the accuracy of the moist model we will utilise the moist benchmark simulation proposed in Bryan and Fritsch (2002). This testcase was previously implemented by the author using the $\mathrm{PI}_m^{p_0}$ model in O'Neill and Klein (2013). In the present work we will examine how the $\mathrm{PI}_m^{\mathrm{tc},p_0}$ model preforms and observe the possible differences between present results and the ones outlined in O'Neill and Klein (2013).

The benchmark testcase consists of a saturated and neutrally stratified hydrostatic atmosphere at rest with an initially constant value for the total water mixing ratio of 0.02 and a constant base value for the wet equivalent potential temperature $\theta_e$ of 320 K where $\theta_e$ is defined as as

$$\theta_e = T\left(\frac{p_d}{p_{ref}}\right)^{-R/(c_p+c_{pc}q)} \exp\left(\frac{L_v q_v}{(c_p+c_{pc}q)T}\right) \tag{5.9}$$

which is taken from Emanuel (1994). The domain is 20 km wide and 10 km high with solid-wall boundary conditions.

A perturbation of warm air is placed near the bottom of the domain and is

given as

$$\theta^{'} = 2\cos^2\left(\frac{\pi R}{2}\right) \tag{5.10}$$

where

$$R = \sqrt{\left(\frac{x}{x_r}\right)^2 + \left(\frac{z - z_0}{z_r}\right)^2}, \tag{5.11}$$

$z_0 = 2.0$ km and $x_r = z_r = 2.0$ km. Using equations (3.12), (3.40), (4.16) and (5.9) we can calculate the vertical profiles of $\rho$, $p$, $\theta_q$, $q_v$ and $q_c$ in an iterative fashion given our prescribed values for $q$ and $\theta_e$.

In Bryan and Fritsch (2002) four different compressible equation sets are used. To make a comparison we will look at the one which most closely resembles our own model assumptions which is the one labelled set A. This set uses the same governing equations and evolution equation for potential temperature as were used to derive our $\mathrm{PI}_m^{\mathrm{tc},p_0}$ model and are given by the equations (3.6) and (3.8).

In the original paper the plots of $\theta_e$ and the vertical velocity are used to test model validity and here we will do the same. Below the plots produced from the $\mathrm{PI}_m^{\mathrm{tc},p_0}$ model can be seen in figures (5.12) and (5.13). These figures were produced using CFL = 0.5 with an upper timestep limit of 5 s and using a 100 m grid spacing in the horizontal and vertical directions.

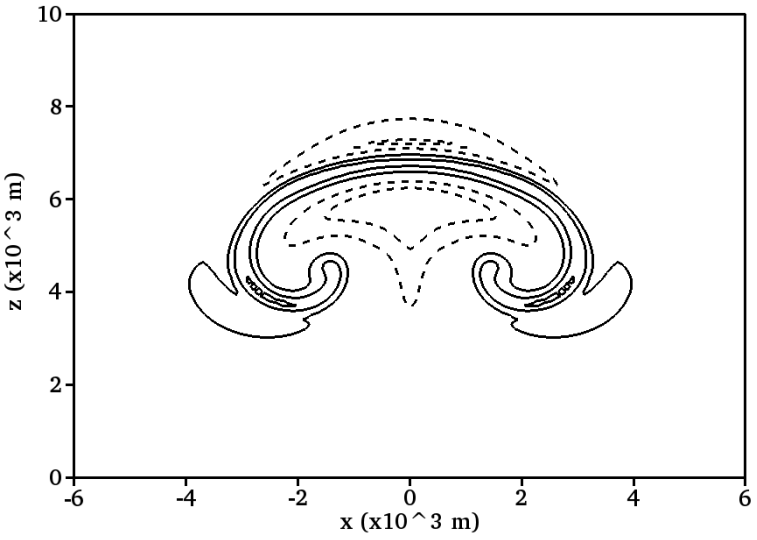


Figure 5.12: A contour plot of the perturbation of the wet equivalent potential temperature at $t = 1000$ s for the $\mathrm{PI}_m^{\mathrm{tc},p_0}$ moist bubble simulation where the contour interval is 0.5 K, the grid spacing is 100 m and the zero contour is omitted.

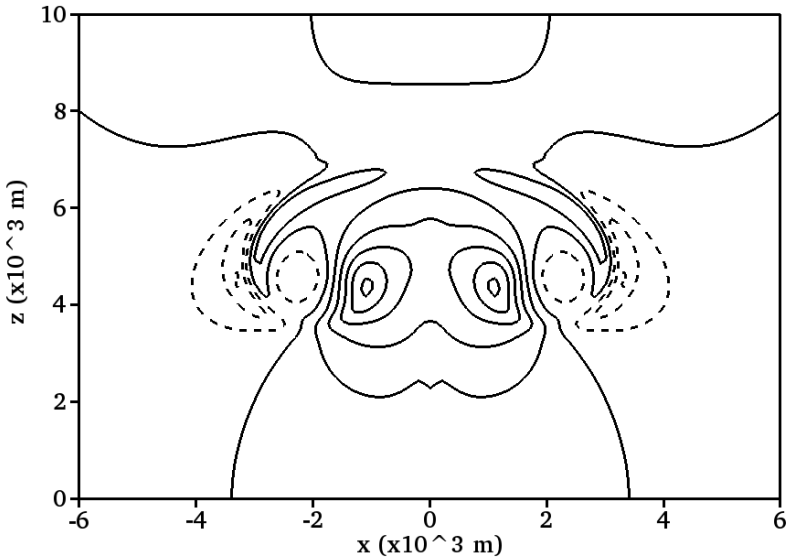


Figure 5.13: A contour plot of the vertical velocity at $t = 1000$ s for the $\mathrm{PI}_m^{\mathrm{tc},p_0}$ moist bubble simulation where the contour interval is 2 $\mathrm{m\,s^{-1}}$ and the grid spacing is 100 m.

These results compare well qualitatively with those in the original paper Bryan and Fritsch (2002), but there are some differences as seen in Table 5.5. Our bubble top rises to about 6.95 km which is slightly higher than the height reached in the original paper of about 6.9km. Looking at the maximum and minimum values we can see that between the wet equivalent potential temperature perturbations there is a variation of about 14% in the case of the maximum values and a 4% variation in the case of the minimum values and between the vertical velocities there is about a 12% variation in the maximum values and a 10% variation in the minimum values compared to the values in the original paper.

Comparing the the $\mathrm{PI}_m^{\mathrm{tc},p_0}$ and $\mathrm{PI}_m^{p_0}$ model results in Table 5.5 we can see a negligible difference between the maximum and minimum values of $\theta_e$ and $w$ but, as for the dry rising bubble testcase in Section 5.2.1, the $\mathrm{PI}_m^{\mathrm{tc},p_0}$ shows improved results for the both the bubble height and bubble width.

There are many differences in our numerics which could account for the discrepancies between our results and the ones presented in Bryan and Fritsch (2002). For example, our equations are solved in conservation form unlike those in the original paper, our codes use different functions to calculate the condensation rate numerically and they have different advection schemes.

In Straka et al. (1993) various models were shown to have large variations in performance when the grid resolution is changed. This illustrated that the numerics have a large role to play in model output. In our case, when we ran the model with a 50% higher grid spacing of in the horizontal and vertical directions (i.e. a grid spacing of 50 m) we found that the maximum and minimum values had much better agreement and some of the qualitative differences in the vertical velocity plot were corrected as shown in Figures (5.14), (5.15) and Table 5.5. In light of this, we can see that even small adjustments to the numerics can influence the overall result and our plots and the ones contained in Bryan and

Fritsch (2002) compare well considering their many numerical differences.

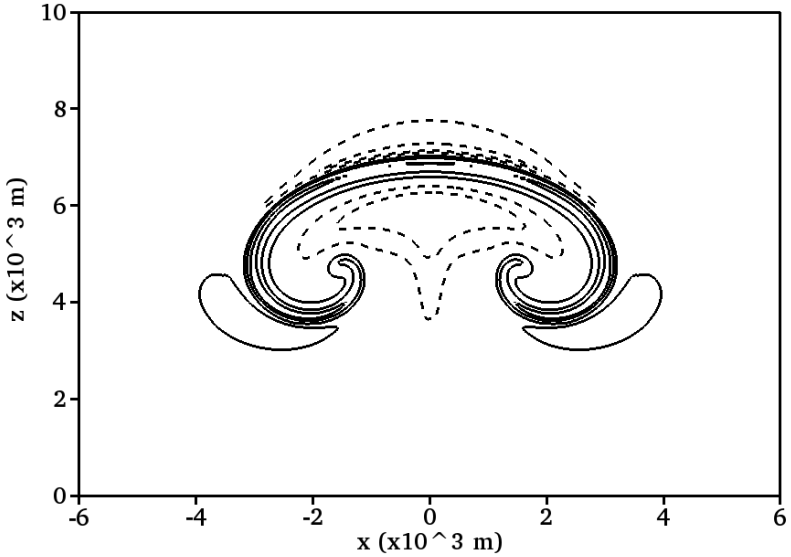


Figure 5.14: A contour plot of the perturbation of the wet equivalent potential temperature at $t = 1000$ s for the $\mathrm{PI}_m^{\mathrm{tc},p_0}$ moist bubble simulation where the contour interval is 0.5 K, the grid spacing is 50 m and the zero contour is omitted.

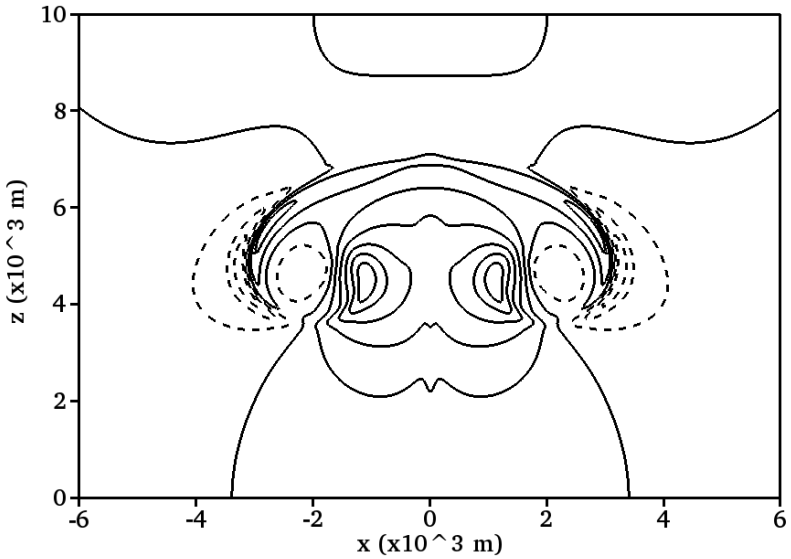


Figure 5.15: A contour plot of the vertical velocity at $t = 1000$ s for the $\mathrm{PI}^{\mathrm{tc}}$ moist bubble simulation where the contour interval is 2 $\mathrm{m\,s^{-1}}$ and the grid spacing is 50 m.

| | $\theta'_{\max}$ | $\theta'_{\min}$ | $w_{\max}$ | $w_{\min}$ | $z_{\text{front}}$ | $x_{\text{right}} - x_{\text{left}}$ |
|---|---|---|---|---|---|---|
| REF | 2.14 K | -1.4 K | 11.88 m s−2 | -7.23 m s$^{-2}$ | 6.9 km | $\approx$ 2.2 km |
| $\text{PI}_m^{\text{tc},p_0}$ | 1.85 K | -1.35 K | 10.41 m s−2 | -6.51 m s−2 | 6.95 km | 2.24 km |
| $\text{PI}_m^{\text{tc},p_0}$ high-res | 2.05 K | -1.37 K | 11.71 m s$^{-2}$ | -7.78 m s$^{-2}$ | 7.02 km | 2.26 km |
| $\text{PI}_m^{p_0}$ | 1.84 K | -1.4 K | 10.96 m s−2 | -6.7 m s−2 | 7.1 km | 1.96 km |

Table 5.5: Table of the maximum and minimum perturbations of potential temperature, vertical velocity and the bubble height $z_{\text{front}}$ and bubble width $x_{\text{right}} - x_{\text{left}}$ at final time $T = 1000$ s for the moist bubble testcase for the reference results in Bryan and Fritsch (2002) (REF), our $\text{PI}_m^{\text{tc},p_0}$ results, our results at a higher resolution ($\text{PI}_m^{\text{tc},p_0}$ high-res) and the results in O'Neill and Klein (2013) ($\text{PI}_m^{p_0}$).

### 5.3.2 Moist thermal in stratified environment

In the moist thermal testcase we will examine the effect of the pressure choice in the microphysical numerics as in Kurowski et al. (2013). Unlike all the previous simulations the results presented here are the preliminary results and, as such, represent a work-in-progress.

The hydrostatically balanced initial profiles of potential temperature, temperature and pressure are taken from Grabowski and Clark (1991) and are written as

$$\theta_0 = \theta_{00} \exp(Sz) \tag{5.12}$$

$$T_0 = \theta_{00} \exp(Sz) \left[1 - \frac{g}{c_p \theta_0 S}(1 - \exp(-Sz))\right] \tag{5.13}$$

$$p_0 = p_{00} \left[1 - \frac{g}{c_p \theta_0 S}(1 - \exp(-Sz))\right]^{c_p/R} \tag{5.14}$$

where $S = 1.3 \times 10^{-5}\text{m}^{-1}$, $\theta_{00} = 296.46$ K and $p_{00} = 850$ hPa. The mixing ratios are calculated from $T$ and $p$ by assuming a constant relative humidity of 20% and the velocities are initially zero. The domain is 3.8 km wide, 4 km high and a constant grid-box size of 10 m is used in both the vertical and horizontal directions. Unlike the testcase presented in 5.3.1 the initial state here is unsaturated and it is not defined in terms of the wet equivalent potential temperature. In general, this is arguably a more realistic testcase than the one presented in the previous section.

The initial temperature perturbation is constrained to a 300m radius which is centered horizontally and whose center is at a height of 800m from the base of the domain. The air within 200m of the bubble center is saturated and the relative humidity gradually approaches the background value as we go farther from the center. We define the perturbation as

$$\begin{aligned} &q_v = q_{vs}, && 0 \le r \le 200\text{m} \\ &q_v = \left[0.2 + (1 - 0.2)\cos^2\left(\tfrac{\pi}{2}\left(\tfrac{r-200}{100}\right)\right)\right] q_{vs}, && 200\text{m} \le r \le 300\text{m} \\ &\theta = \theta_0 + d\theta, && 0 \le r \le 200\text{m} \\ &\theta = \left[\theta_0 + d\theta \cos^2\left(\tfrac{\pi}{2}\left(\tfrac{r-200}{100}\right)\right)\right] q_{vs}, && 200\text{m} \le r \le 300\text{m} \end{aligned} \tag{5.15}$$

where $d\theta = \{0.5\text{ K}, 5\text{ K}, 50\text{ K}\}$ and $q_{vs}$ is calculated using (4.16). Finally, the density is calculated from $\theta$, $p$ and $q_v$ using the equation of state given by (3.23).

A table of the timestep used for each perturbation size for CFL = 0.9 is given in Table 5.6. For each of the three perturbation sizes our models are able to utilize bigger timesteps than the anelastic model presented in Kurowski et al. (2013) with the difference increasing with the increasing perturbation size. This is as expected as the pseudo-incompressible approximation has been shown to have greater validity than the analestic approximation for large temperature perturbations, see Durran (1989) and Klein et al. (2010).

| | 0.5 K | 5 K | 50 K |
|---|---|---|---|
| $\mathrm{PI}_m^{\mathrm{tc},p_0}$, $\mathrm{PI}_m^{\mathrm{tc},p}$ $\Delta t_{max}$ | 74 s | 23 s | 2 s |
| $\mathrm{PI}_m^{\mathrm{tc},p_0}$, $\mathrm{PI}_m^{\mathrm{tc},p}$ $\Delta t$ | 2.26 s | 0.88 s | 0.25 s |
| REF $\Delta t$ | 2.0 s | 0.5 s | 0.02 s |

Table 5.6: Timestep choices for the $\mathrm{PI}_m^{\mathrm{tc},p_0}$ and $\mathrm{PI}_m^{\mathrm{tc},p}$ models and the reference anelastic model taken from Kurowski et al. (2013) (REF). The $\mathrm{PI}_m^{\mathrm{tc},p_0}$ and $\mathrm{PI}_m^{\mathrm{tc},p}$ $\Delta t$ is an average of the utilised variable timestep.

The simulation results are shown in the contour plots in Figures 5.16-5.18 and the timeseries plots in Figures 5.19-5.22. Note, the tick marks in the contour plots were chosen to match those of Kurowski et al. (2013). Some observations that are immediately apparent when the plots are compared with those in Kurowski et al. (2013) are that our $q_t$ contour plots contain much more small scale details, much more contour levels and, also, our bubbles rise to a much lower height. The differences between our results are thought to originate from the many uncertainties in the initial condition set-up of the testcase, e.g. constant values and pressure initialisation. A number of these uncertainties are outlined in Appendix C. It is also important to note that the plots for the 50K runs for the $\mathrm{PI}_m^p$ model are not shown due to the fact that the pressure becomes unstable during the simulation. This could mean that only the $\mathrm{PI}_m^{p_0}$ model is applicable for a large potential temperature perturbations and it may indicate a potential weak point in our model.

However, there are some encouraging aspects to the results. For example, although the bubble height is, in general, too low, the contour plots of $p$ and $w$ and the timeseries plots look qualitatively similar to the original plots. Also, we are now able to run our model, at least for reasonable temperature perturbations, using the full pressure in the microphysics.

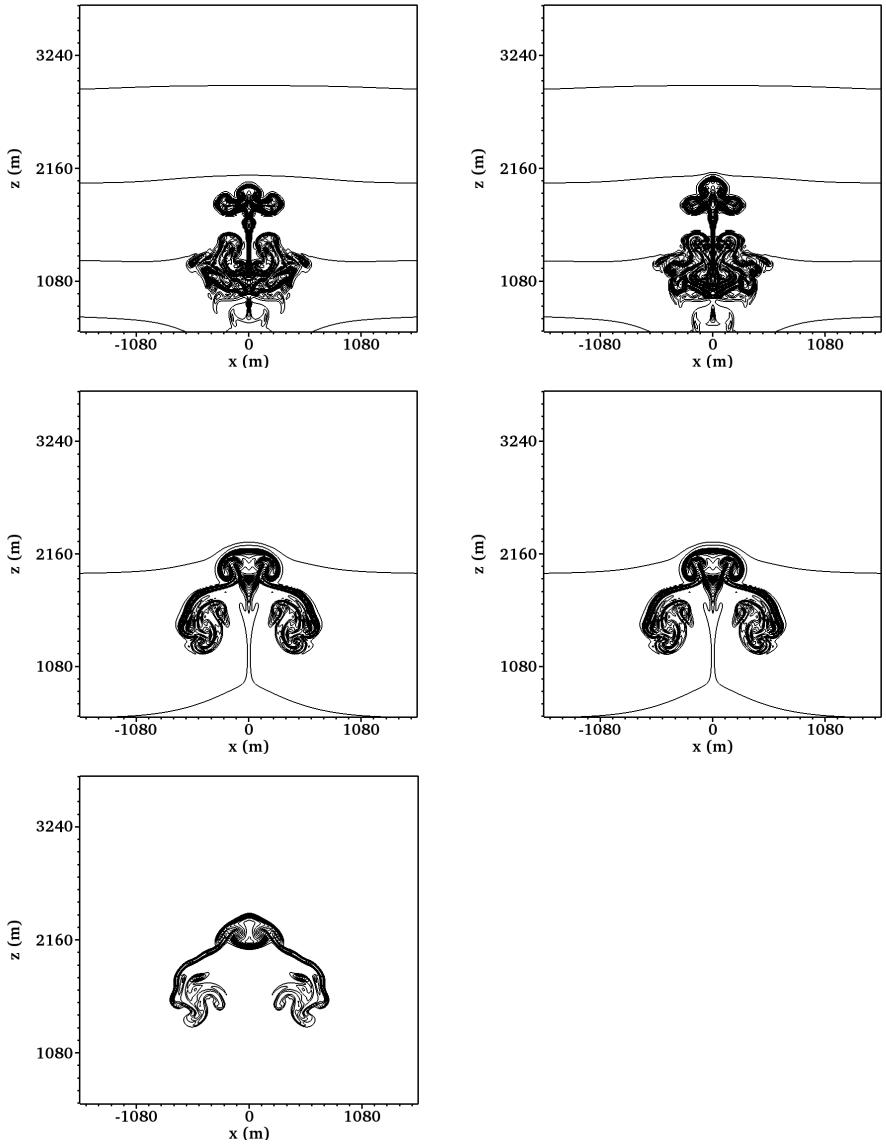


Figure 5.16: Contour plot of the total mixing ratio $q$ for the moist thermal testcase with a 0.5 K (top, contour interval 0.25, $t = 950$ s), 5 K (middle, contour interval 0.5, $t = 300$ s) and 50 K (bottom, contour interval 0.12, $t = 95$ s) initial perturbation for the $\mathrm{PI}_m^{\mathrm{tc},p_0}$ model (left) and the $\mathrm{PI}_m^{\mathrm{tc},p}$ model (right).

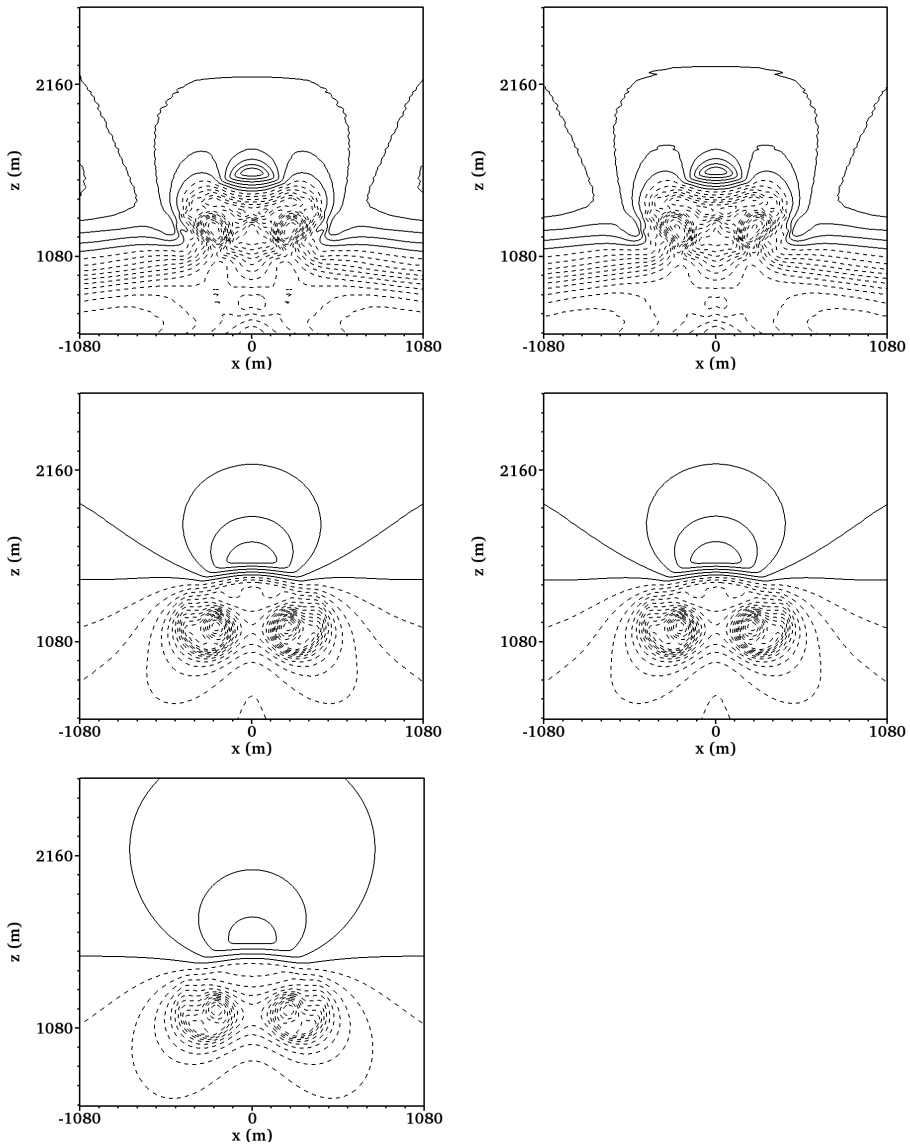


Figure 5.17: Contour plot of the pressure perturbation for the moist thermal testcase with a 0.5 K (top, contour interval 0.5, $t = 475$ s), 5 K (middle, contour interval 4, $t = 150$ s) and 50 K (bottom, contour interval 60, $t = 47.5$ s) initial perturbation for the $\mathrm{PI}_m^{\mathrm{tc},p_0}$ model (left) and the $\mathrm{PI}_m^{\mathrm{tc},p}$ model (right). Solid lines correspond to positive values and the dashed lines correspond to negative values.

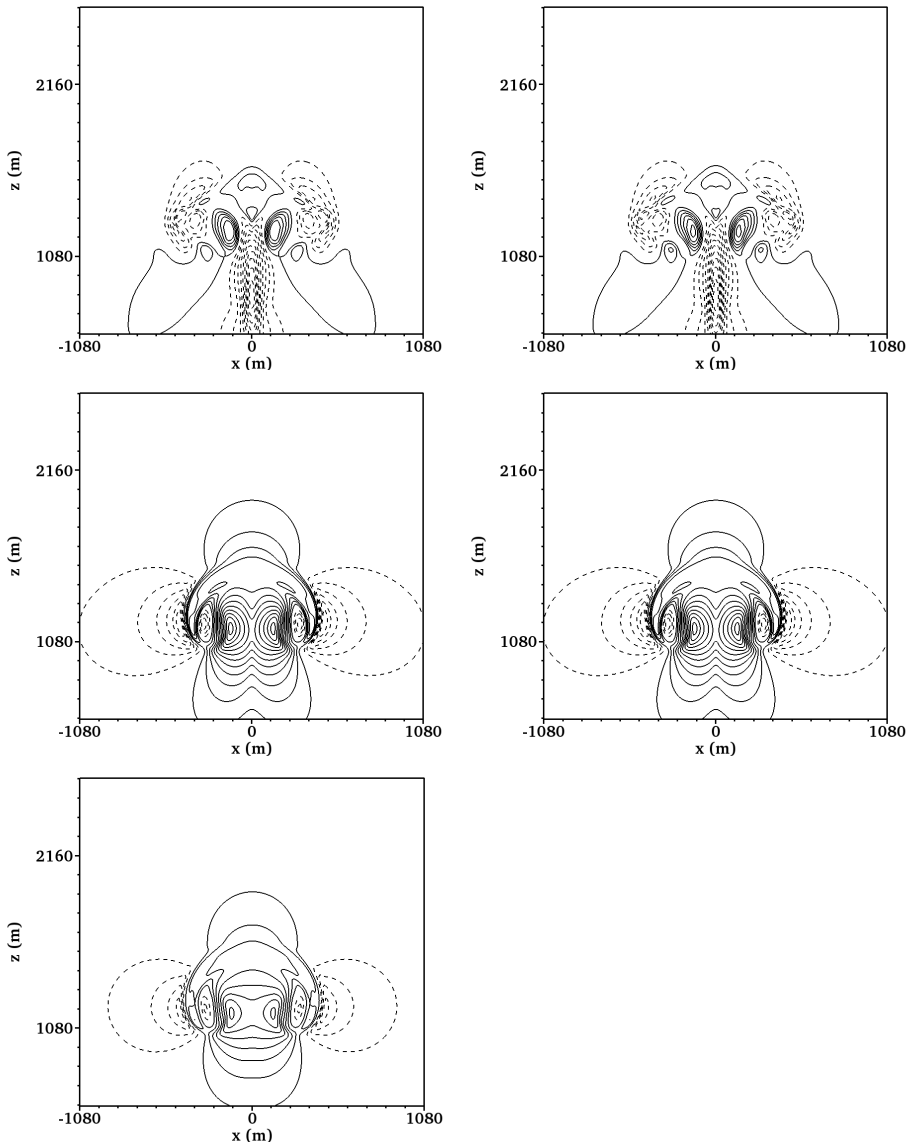


Figure 5.18: Contour plot of the vertical velocity for the moist thermal test-case with a 0.5 K (top, contour interval 0.5, $t = 475$ s), 5 K (middle, contour interval 1, $t = 150$ s) and 50 K (bottom, contour interval 5, $t = 47.5$ s) initial perturbation for the $\mathrm{PI}_m^{\mathrm{tc},p_0}$ model (left) and the $\mathrm{PI}_m^{\mathrm{tc},p}$ model (right). Solid lines correspond to positive values and the dashed lines correspond to negative values.

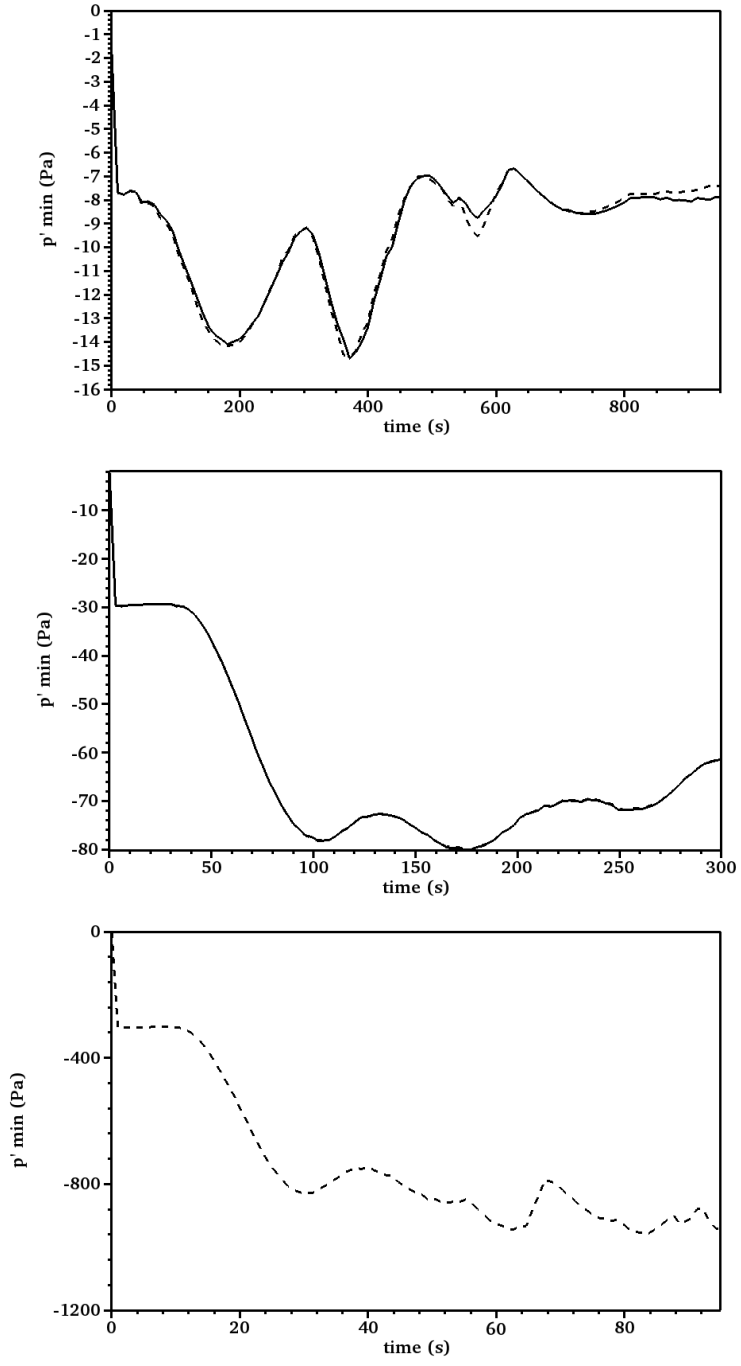


Figure 5.19: Timeseries for the minimum pressure perturbation for the moist thermal testcase with a 0.5 K (top), 5 K (middle) and 50 K (bottom) initial perturbation for the $\mathrm{PI}_m^{\mathrm{tc},p_0}$ model (dashed) and the $\mathrm{PI}_m^{\mathrm{tc},p}$ model (solid).

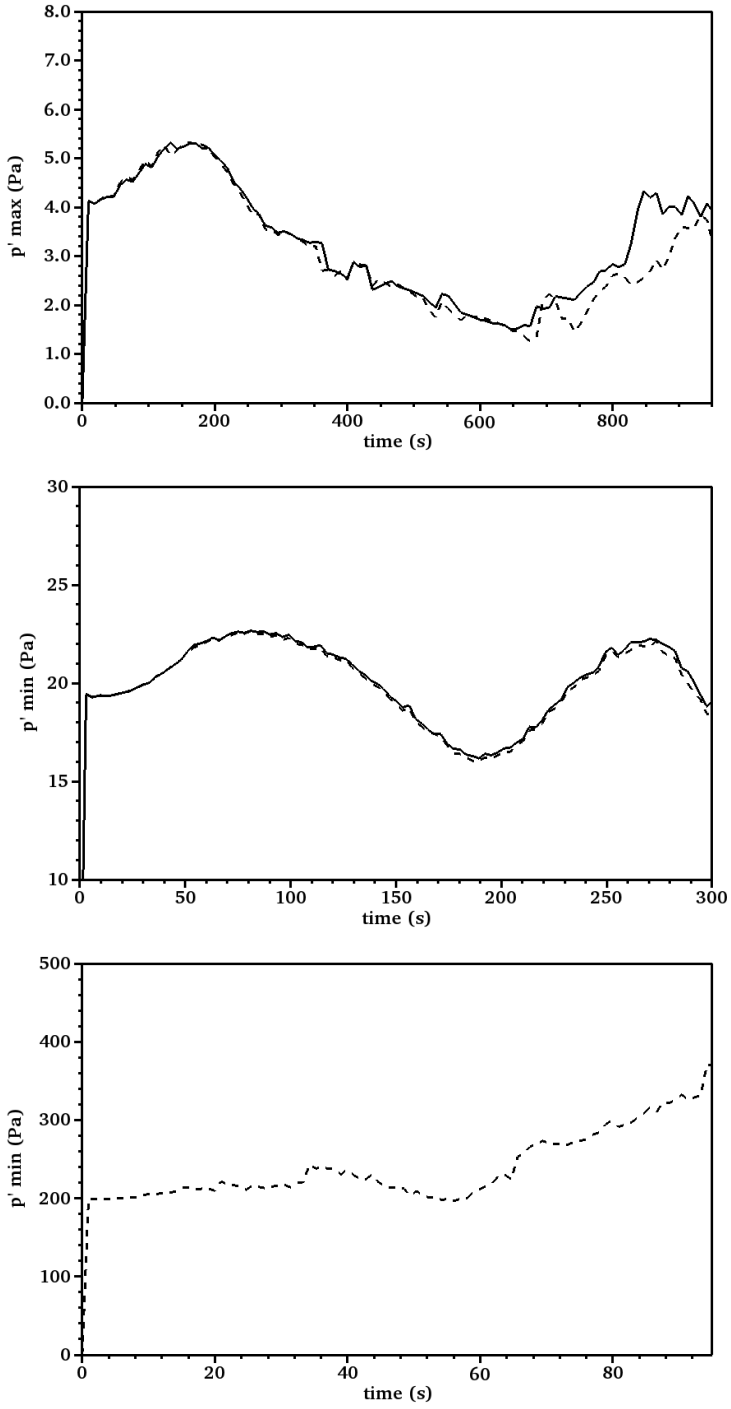


Figure 5.20: Timeseries for the maximum pressure perturbation for the moist thermal testcase with a 0.5 K (top), 5 K (middle) and 50 K (bottom) initial perturbation for the $\mathrm{PI}_m^{\mathrm{tc},p_0}$ model (dashed) and the $\mathrm{PI}_m^{\mathrm{tc},p}$ model (solid).

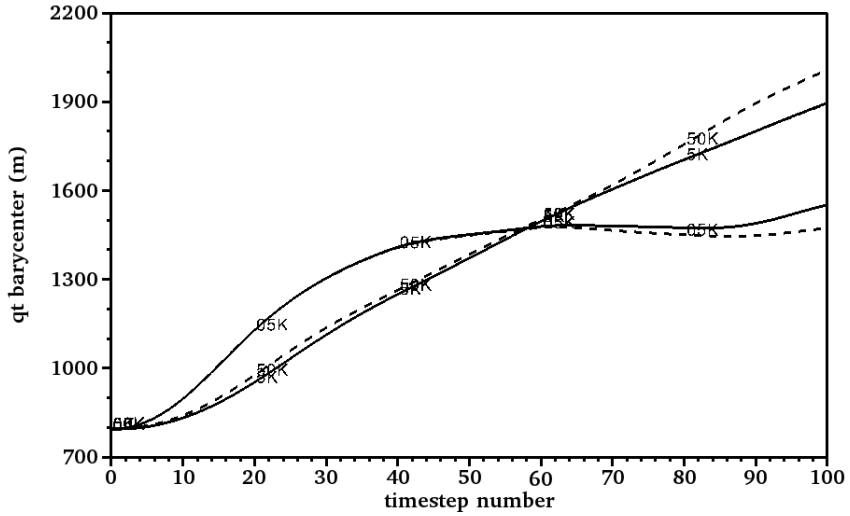


Figure 5.21: Timeseries for the total mixing ration barycenter for the moist thermal testcase for each initial potential temperature perturbation for the $\mathrm{PI}_m^{\mathrm{tc},p_0}$ model (dashed) and the $\mathrm{PI}_m^{\mathrm{tc},p}$ model (solid).

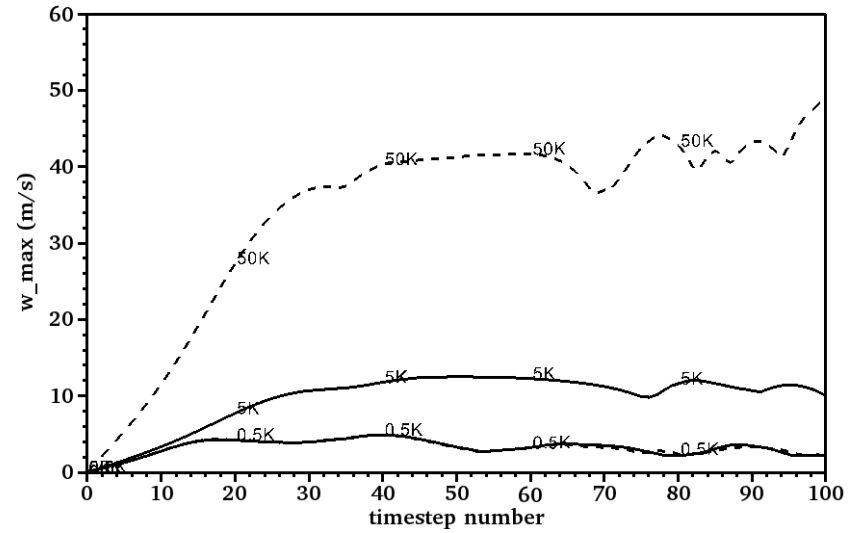


Figure 5.22: Timeseries for the maximum vertical velocity for the moist thermal testcase for each initial potential temperature perturbation for the $\mathrm{PI}_m^{\mathrm{tc},p_0}$ model (dashed) and the $\mathrm{PI}_m^{\mathrm{tc},p}$ model (solid).

# Chapter 6

# Summary

In the preceding pages two extensions to the pseudo-incompressible model are proposed. These extensions are: 1) an alternate form of the model's momentum equation which is written in terms of $p$ and $\rho$ rather than $\pi$ and $\theta$ while retaining thermodynamic consistency and 2) the inclusion of phase changes and diabatic terms.

The alternate "thermodynamically consistent" form of the equations, which was first presented in Klein and Pauluis (2011), is implemented numerically and examined in several testcases. In this form an extra buoyancy term which is dependent on the pressure perturbations is required in order to ensure the momentum equation preserves all terms up to first order in $p'$. To examine the importance of this term we compared the performance of a pseudo-incompressible model which includes this term and one which disregards it on a number of standard testcases by inspecting, e.g., several contour plots and indicative values such as maximum potential temperature perturbation and bubble height at the final time. We found that by retaining the pressure perturbation dependence in the gravity term in the momentum equation the model shows a much better agreement to published compressible results for the same testcases. This was, not surprisingly, particularly important in the buoyancy driven testcases where when the extra term was neglected the bubbles were found to rise too quickly and to a greater height. In the inertia gravity wave testcase the difference between the models was minimal as buoyancy was no longer the driving factor. Further analysis of these results and a comparison with a compressible model which utilises the same numerics is presented in Benacchio et al. (2014).

Whether or not the $\mathrm{PI}^{\mathrm{tc}}$ equation set performs better than the standard form of the pseudo-incompressible model (or the anelastic model) remains to be examined. However, since the models agree up to first order in $p'$, little variation is expected. The only apparent advantage in the dry case is that in our equation set the pressure term in the momentum equation is written in conservative form but this advantage could be negated as a result of our extra buoyancy term.

In deriving the $\mathrm{PI}^{\mathrm{tc}}$ model we have assumed that the pressure perturbations are small but unlike the anelastic equations no constraint was imposed on the size of the potential temperature or density variations. The assumption of small potential temperature and density variations is generally valid for moist atmospheric processes and as a result the $\mathrm{PI}^{\mathrm{tc}}$ model may be expected to be superior to an anelastic model only in specific cases. For example, in cases of deep convection and in the presence of baroclinic waves due to the retention of the baroclinic vorticity production term (see page 33 in Cotton et al. (2011)).

The second main development was to derive a moist thermodynamically consistent pseudo-incompressible model which includes phase changes and diabatic terms. The addition of diabatic terms requires adjustments to the divergence constraint not seen in the more common anelastic model. Borrowing and adapting ideas from Almgren et al. (2008), these issues were tackled by allowing the background state to vary in time and then deriving a set of equations governing the evolution of the background variables. The foundation of this model is presented in O'Neill and Klein (2013) and here we developed it further to also be thermodynamically consistent by following similar methods to the dry case.

Although the derivation of the $\mathrm{PI}^{\mathrm{tc}}$ model was motivated by the findings contained in Almgren et al. (2008) there are some notable differences between the models. In Almgren's work an outflow top boundary is used whereas here we have given a method which is able to impose solid-wall boundary conditions.

Another difference is that we have kept the coefficient in the divergence constraint in a physically meaningful form and did not have to result writing it as an integral. This is due to the fact that the $\gamma$ in the definition of potential temperature is constant. However, the coefficient will have to be written in a similar integral form when a non-constant $\gamma$ is required.

The moist model was shown to perform well against a compressible model for the idealized bubble testcase presented in Bryan and Fritsch (2002). To compare the models contour plots of the vertical velocity and wet equivalent potential temperature are examined. The plots compare well and the extension to thermodynamic consistency was shown to solve the issues of incorrect bubble height and width found in O'Neill and Klein (2013). However, discrepancies in the form of the vertical velocity plot still remain but this variation is thought to stem more from the numerics than the choice of the model equations.

In the second moist testcase the effect of the pressure choice on the condensation rate calculation is examined using moist thermal testcase presented in Kurowski et al. (2013). Unlike the other testcases this aspect remains a work in progress and, as of yet, there is not a good agreement between our model results and the reference anelastic and compressible model results. We remain unsure whether this is a model error or an error in the testcase set-up and more investigation is required. However, these preliminary results point to both an advantage and weak point in our model. The advantage is that we are able to run at much higher timesteps, particulary for larger potential temperature perturbations, than the anelastic and compressible models. The disadvantage is that unlike the reference anelastic model the $\mathrm{PI}_m^p$ model breaks down for the largest potential temperature perturbation and this could mean that only the $\mathrm{PI}_m^{p_0}$ model is applicable to perturbations of this size. Though, until issues with the testcase are solved these preliminary results remain speculative.

In this work we have laid the foundation of the dry and moist thermodynamically consistent models and it is the aim of further work to take advantage of the unique features the models possess, namely, the usage of large timesteps in situations with large potential temperature perturbations and to have a soundproof model which can be used with non-constant heat capacities. The first advantage is already available in the dry case and will be realised in the moist case once the issues with the moist thermal simulation have been resolved. The second advantage will be realised once the model is extend to include more complex equations of state with non-constant values for $\gamma$. To reach the latter goal there are two suggested paths: 1) to follow the methods of Almgren et al. (2008) more closely as stated above or 2) to utilise a variable other than $P$, i.e. the Enthalpy, as the central point of our derivation.

In its present state, however, the model remains of great theoretical interest and gives us further insight into the intricate and interwoven world of soundproof models.

# Acknowledgements

As with all academic research the work presented here was far from a solo effort. The author would like to thank his supervisor Prof Rupert Klein for the guidance, the Berlin Mathematical School for the financial and personal support, Nadja Wisniewski for her dedication, Ann Almgren for the many insightful comments, Tommaso Benacchio for the engaging discussions, the reviewers of both the papers I was involved in for the wonderful feedback, the Lawrence Livermore National Laboratory for the usage of their SAMRAI library, HYPRE library and VisIt visualisation program and the entire AG Klein but especially Michael Oevermann, Stephan Gerber and Matthias Waidmann for their work in developing the fluid flow solver code used in this work.

The author would also like to thank the many supporters outside of his academic life; my loving parents Patrick and Teresa, my brother Byron, my partner Maria and all my close friends.

# Appendices

# Appendix A

# Background density choice in the moist model

Contrary to $\rho_0$ in our moist model the model presented in Almgren et al. (2008) defines $\rho_0$ as the horizontal average of $\rho$ such that

$$\rho = \rho_0 + \rho' \tag{A.1}$$

where $\overline{\rho'} = 0$. By writing the density in this way one can derive an evolution equation for $\rho_0$ by simply taking the average of (3.1) to get

$$(\rho_0)_t + \frac{\partial}{\partial z}\left(\rho_0 w_0 + \overline{\rho' \tilde{w}}\right) = 0 \tag{A.2}$$

which is equivalent to Almgren et al. (2008) equation (29). This is more general than assuming that $\rho_0$ satisfies the conservation of mass as we did in (3.25). In Almgren et al. (2008) they state that in cases with large rates compositional changes failing to define $\rho_0$ as an average can lead to " loss of physical fidelity over time". However, it remains to be tested whether or not defining $\rho_0$ as an average in our model will yield improved results.

# Appendix B

# Moist variable definitions

Definition of constants for the two moist testcases shown in section 5.3.

## B.1 Moist rising bubble constants

A list of the constants taken from Bryan and Fritsch (2002) and used for the testcase in section 5.3.1

$g = 9.81\ \mathrm{m\,s^{-2}}$ - Acceleration due to gravity

$p_{ref} = 1.0 \times 10^5\ \mathrm{Pa}$ - Reference pressure

$T_{ref} = 273.15\ \mathrm{K}$ - Reference temperature

$R = 287\ \mathrm{J\,kg^{-1}\,K^{-1}}$ - Gas constant of dry air

$R_v = 461\ \mathrm{J\,kg^{-1}\,K^{-1}}$ - Gas constant of water vapor

$c_p = 1004.0\ \mathrm{J\,kg^{-1}\,K^{-1}}$ - Specific heat of dry air at constant pressure

$c_{pv} = 1885\ \mathrm{J\,kg^{-1}\,K^{-1}}$ - Specific heat of water vapor at constant pressure

$c_{pc} = 4186\ \mathrm{J\,kg^{-1}\,K^{-1}}$ - Specific heat of cloud water at constant pressure

$c_v = 717\ \mathrm{J\,kg^{-1}\,K^{-1}}$ - Specific heat of dry air at constant volume

$L_{v0} = 2.5 \times 10^6\ \mathrm{J\,kg^{-1}}$ - Latent heat of vaporisation reference value

$L_v = L_{v0} - (c_{pc} - c_{pv})\,(T - T_{ref})$ - Latent heat of vaporisation

## B.2 Moist thermal constants

A list of the constants taken from Kurowski et al. (2013) and used for the testcase in section 5.3.2

$g = 9.80616\ \mathrm{m\,s^{-2}}$ - Acceleration due to gravity

$p_{ref} = 1.0 \times 10^5\ \mathrm{Pa}$ - Reference pressure

$T_{ref} = 273.16\ \mathrm{K}$ - Reference temperature

$R = 287.04\ \mathrm{J\,kg^{-1}\,K^{-1}}$ - Gas constant of dry air

$R_v = 461\ \mathrm{J\,kg^{-1}\,K^{-1}}$ - Gas constant of water vapor

$c_p = 1004.0\ \mathrm{J\,kg^{-1}\,K^{-1}}$ - Specific heat of dry air at constant pressure

$c_{pv} = 1885\ \mathrm{J\,kg^{-1}\,K^{-1}}$ - Specific heat of water vapor at constant pressure

$c_{pc} = 4186\ \mathrm{J\,kg^{-1}\,K^{-1}}$ - Specific heat of cloud water at constant pressure

$c_v = 717\ \mathrm{J\,kg^{-1}\,K^{-1}}$ - Specific heat of dry air at constant volume

$L_v = L_{v0} = 2.53 \times 10^6\ \mathrm{J\,kg^{-1}}$ - Latent heat of vaporisation

# Appendix C

# Moist thermal initial condition uncertainties

At the time of writing there are several uncertainties in the exact model set-up outlined in Grabowski and Clark (1991) and utilised in Kurowski et al. (2013). For example, through personal communication with the author it became apparent that the reference pressure and the base pressure intentionally do not match ($p_{00} = 850$ hPa and $p_{ref} = 1000$ hPa). However, when initialised with the same value for both $p_{00}$ and $p_{ref}$ a much better agreement in the initial values for $q_t$ is achieved (these values correspond to the contours intersecting with the vertical axes in Figure 5.16).

Also, through further personal communication it became known that there is a difference between the temperature initialization in Grabowski and Clark (1991) and Kurowski et al. (2013). The former uses the (5.13) for the temperature initialisation whereas the latter uses

$$T_0 = \theta_{00} \exp(Sz) \left[1 - \frac{g}{c_p T_{00} S}(1 - \exp(-Sz))\right] \tag{C.1}$$

with $T_{00}$ in the brackets instead of $\theta_{00}$. However, when this change was implemented no improvement was seen in the results.

# Appendix D

# Zusammenfassung

Die Atmosphärenströme definieren sich durch Prozesse auf unterschiedlichsten zeitlichen wie räumlichen Skalen. Diese Prozesse können mit den "kompressiblen" Navier-Stokes Gleichungen modelliert werden. Es ist anzunehmen, dass eine Nichtberücksichtigung von Schallwellen zu numerischen Vereinfachungen führt. Dies ist auch von theoretischem Interesse. Speziell unter schallfreien Bedingungen wurde eine Reihe von Gleichungen entwickelt, sog. "schallfreie Gleichungen", welche das Problem der Schallwellefilterung lösen.

Ein Lösungsweg beschreibt die "pseudo-inkompressiblen Gleichungen", welche der Fokus dieser Arbeit darstellt. Die pseudo-inkompressible Annäherung definiert die Dichte als eine Funktion von hydrostatischem Druck und Temperatur. Diese Annäherung resultiert in einer Divergenz-Gleichung, die, im Gegensatz zur Evolutions-Gleichung, Schalleffekte im Modell vernachlässigbar macht.

Die Studie entwickelt die pseudo-inkompressible Annäherung in zwei Richtungen weiter: 1) Implementierung einer "thermodynamisch konsistenten" Form in die pseudo-inkompressiblen Gleichungen und 2) die Expandierung des Modellraums, um diabetische Terme und Phasenübergange modellieren zu können.

Die numerische Implementierung der "thermodynamisch konsistenten" Form und der Modellexpandierung stellt eine "in-house" Entwicklung von pseudo-inkompressiblen Finite-Volumen-Routinen dar. Nach der Implementierung werden standardisierte Teststudien durchgeführt und die Ergebnisse mit anderen Modellen verglichen.

# Bibliography


Achatz, U., Klein, R., Senf, F., 2010. Gravity waves, scale asymptotics and the pseudo-incompressible equations. Journal of Fluid Mechanics 663, 120–147.

Almgren, A. S., 2000. A new look at the pseudo-incompressible solution to lamb's problem of hydrostatic adjustment. Journal of the Atmospheric Sciences 57, 995–998.

Almgren, A. S., Bell, J. B., C. A. Rendleman, ., Zingale, M., 2006a. Low mach number modeling of type ia x-ray supernovae i. hydrodynamics. The Astrophysical Journal 637, 922–936.

Almgren, A. S., Bell, J. B., C. A. Rendleman, ., Zingale, M., 2006b. Low mach number modeling of type ia x-ray supernovae ii. energy evolution. The Astrophysical Journal 649, 927–938.

Almgren, A. S., Bell, J. B., C. A. Rendleman, ., Zingale, M., 2008. Low mach number modeling of type ia x-ray supernovae iii. reactions. The Astrophysical Journal 684, 449–470.

Bannon, P. R., 1996. On the anelastic approximation for a compressible atmosphere. Journal of the Atmospheric Sciences 53, 3618–3628.

Bannon, P. R., 2002. Theoretical foundations for models of moist convection. Journal of Atmospheric Science 59, 1967–1982.

Batchelor, G. K., 1967. An introduction to fluid dynamics. Cambridge University Press.

Bell, J. B., Marcus, D. L., 1992. A second-order projection method for variable-density flows. Journal of Computational Physics 101, 334–348.

Benacchio, T., O'Neill, W. P., Klein, R., 2014. A blended soundproof-to-compressible numerical model for small to meso-scale atmospheric dynamics. Monthly Weather Review 142, 4416–4438.

Bolton, D., 1980. The computation of equivalent potential temperature. Monthly Weather Review 108, 1046–1053.

Botta, N., Klein, R., Langenberg, S., Lützenkirchen, S., 2004. Well balanced finite volume methods for nearly hydrostatic flows. Journal of Computational Physics 196, 539–565.

Boussinesq, J. V., 1903. Théorie des Analytique de la Chaleur. Vol. 2. Gauthier-Villars.

Bryan, G. H., Fritsch, J. M., Dec. 2002. A benchmark simulation for moist nonhydrostatic numerical models. Mon. Wea. Rev. 130 (12), 2917–2928.

Clark, T. L., Jun. 1977. A small-scale dynamic model using a terrain-following coordinate transformation. Journal of Computational Physics 24, 186–215.

Clark, T. L., 1979. Numerical simulations with a three-dimensional cloud model: Lateral boundary condition experiments and multicellular severe storm simulations. Journal of Atmospheric Sciences 36, 2191–2215.

Cotton, W. R., Bryan, G., van der Heever, S. C., 2011. Storm and Cloud Dynamics. Academic Press.

Dudhia, J., 1993. A nonhydrostatic version of the penn state/ncar mesoscale model: Validation tests and simulation of an atlantic cyclone and cold front. Monthly Weather Review 121, 1493–1513.

Durran, D., 1989. Improving the anelastic approximation. Journal of the Atmospheric Sciences 49, 1453–1461.

Durran, D. R., 2008. A physically motivated approach for filtering acoustic waves from the equations governing compressible stratified flow. Journal of Fluid Mechanics 601, 365–379.

Emanuel, K. A., 1994. Atmospheric Convection. Oxford University Press.

Falgout, R., Yang, U., 2002. hypre: A library of high performance preconditioners. In: Sloot, P., Hoekstra, A., Tan, C., Dongarra, J. (Eds.), Computational Science — ICCS 2002. Vol. 2331 of Lecture Notes in Computer Science. Springer Berlin Heidelberg, pp. 632–641.

Ferziger, J. H., Perić, M., 2002. Computational Methods for Fluid Dynamics. Springer-Verlag.

Gottlieb, S., Shu, C.-W., Tadmor, E., 2001. Strong stability-preserving high-order time discretization methods. SIAM Review 43, 89–112.

Grabowski, W. W., Clark, T. L., 1991. Cloud–environment interface in- stability: Rising thermal calculations in two spatial dimen- sions. Journal of Atmospheric Sciences 48, 527–546.

Grabowski, W. W., Smolarkiewicz, P. K., 1990. Monotone finite-difference approximations to the advection-condensation problem. Monthly Weather Review 118, 2082–2097.

Grabowski, W. W., Smolarkiewicz, P. K., 2002. A multiscale anelastic model for meteorological research. Monthly Weather Review 130, 939–956.

Klassen, G. P., Clark, T. L., 1985. Dynamics of the cloud-environment interface and entrainment in small cumuli: Two-dimensional simulations in the absence of ambient shear. Journal of the Atmospheric Sciences 42, 2621–2642.

Klein, R., 2009. Asymptotics, structure, and integration of sound-proof atmospheric flow equations. Theoretical and Computational Fluid Dynamics 23, 161–195.

Klein, R., Achatz, U., Bresch, D., Knio, O. M., Smolarkiewicz, P. K., 2010. Regime of validity of soundproof atmospheric flow models. Journal of Atmospheric Sciences 67, 3226–3237.

Klein, R., O'Neill, W. P., Benacchio, T., Vater, S., 2013. Scale-dependent time integration for weakly compressible atmospheric flows. Proceedings of the ECMWF Seminar 863 on Numerical Methods.

Klein, R., Pauluis, O., 2011. Thermodynamic consistency of a pseudo-incompressible approximation for general equations of state. Journal of the Atmospheric Sciences 69, 961–968.

Klemp, J. B., Wilhelmson, R. B., 1978. The simulation of three- dimensional convective storm dynamics. Journal of Atmospheric Sciences 35, 1070–1096.

Kurowski, M. J., Grabowski, W. W., Smolarkiewicz, P. K., 2013. Towards multiscale simulation of moist flows with soundproof equations. Journal of the Atmospheric Sciences (early online release).

LeVeque, R. J., 1992. Numerical Methods for Conservation Laws. Birkhäuser Verlag.

LeVeque, R. J., 2002. Finite-Volume Methods for Hyperbolic Problems. Cambridge University Press.

Lipps, F. B., Helmer, R. S., 1982. A scale analysis of deep moist convection and some related numerical calculations. Journal of Atmospheric Sciences 29, 2192–2210.

Lipps, F. B., Helmer, R. S., 1986. Numerical simulation of deep tropical convection associated with large-scale convergence. Journal of Atmospheric Sciences 43, 1796–1816.

Majda, A., 2003. Introduction to PDEs and Waves for the Atmosphere and Ocean. Courant Lecture Notes in Mathematics.

Nonaka, A., Almgren, A. S., Bell, J. B., Lijewski, M. J., Malone, C. M., Zingale, M., 2010. MAESTRO: An adaptive low Mach number hydrodynamics algorithm for stellar flows. The Astrophysical Journal Supplement Series 188, 358–383.

Ogura, Y., Phillips, N. A., 1962. Scale analysis of deep and shallow convection in the atmosphere. Journal of Atmospheric Sciences 19, 173–179.

O'Neill, W. P., Klein, R., 2013. A moist pseudo-incompressible model. Atmospheric Research.

Pauluis, O., 2008. Thermodynamic consistency of the anelastic approximation for a moist atmosphere. Journal of the Atmospheric Sciences 65, 2719–2729.

Pedlosky, J., 1979. Geophysical Fluid Dynamics. Springer-Verlag.

Pruppacher, H. R., Klett, J. D., 1997. Microphysics of Clouds and Precipitation. Kluwer Academic Publishers.

Restelli, M., Giraldo, F. X., 2009. A conservative discontinuous galerkin semi-implicit formulation for the navier–stokes equations in nonhydrostatic mesoscale modeling. SIAM Journal of Scientific Computing 31, 2231–2257.

Rogers, R. R., Yau, M. K., 1976. A Short Course in Cloud Physics. Butterworth-Heinemann.

Schneider, T., Botta, N., Geratz, K. J., Klein, R., 1999. Extension of finite volume compressible flow solvers to multi-dimensional, variable density zero Mach number flows. Journal of Computational Physics 155, 248–286.

Skamarock, W. C., Klemp, J. B., 1994. Efficiency and accuracy of the klemp-wilhelmson time-splitting technique. Monthly Weather Review 122, 2623–2630.

Smolarkiewicz, P., Charbonneau, P., 2013. EULAG, a computational model for multiscale flows: An MHD extension. Journal of Computatiional Physics 236, 608–623.

Smolarkiewicz, P., Kühnlein, C., Wedi, N., 2014. A consistent framework for discrete integrations of soundproof and compressible PDEs of atmospheric dynamics. Journal of Computatiional Physics 263, 185–205.

Smolarkiewicz, P. K., Dörnbrack, A., 2008. Conservative integrals of adiabatic Durran's equations. International Journal for Numerical Methods in Fluids 56, 1513–1519.

Straka, J. M., Wilhelmson, R. B., Wicker, L. J., Anderson, J. R., Droegemeier, K. K., Jul. 1993. Numerical solutions of a non-linear density current: A benchmark solution and comparisons. International Journal for Numerical Methods in Fluids 17, 1–22.

Vallis, G., 2006. Atmospheric and Oceanic Fluid Dynamics. Cambridge University Press.

Vater, S., Klein, R., 2009. Stability of a cartesian grid projection method for zero Froude number shallow water flows. Numerische Mathematik 113, 123–161.